Voxel-based additive manufacturing of biomimetic hard-soft materials

A fundamental study on the effect of biomimetic design parameters on fracture properties

Maike Edens | Master thesis | June 2018



TU Delft

Voxel-based additive manufacturing of biomimetic hard-soft materials

A fundamental study on the effect of biomimetic design parameters on fracture properties

by

Maike Edens

to obtain the degree of Master of Science
at the Delft University of Technology,
to be defended on Thursday June 14, 2018 at 10:00 AM.

Student number:	4162323	
Thesis committee:	Prof. dr. A. A. Zadpoor	TU Delft, supervisor
	Dr. M. J. Mirzaali	TU Delft, supervisor
	Dr. J. Zhou	TU Delft
	Dr. ir. G. Smit	TU Delft

This thesis is confidential and cannot be made public until June 14, 2019.

TU Delft

Preface

After obtaining my bachelor degree in Industrial Design I decided to study Biomedical Engineering due to my interest in the medical world, and material and mechanical engineering. During my masters, I got passionate about what additive manufacturing (AM) can do for the medical world, in particular for biomaterials and implants. Hence, I am really grateful to got the opportunity to work with an advanced 3D printer during my master thesis. The Objet500 Connex3 Polyjet printer, that I have used during my thesis, is able to simultaneously print multiple materials at micrometer scale. This printer enables the rapid manufacturing of biomimetic hard-soft materials, which is the subject of my thesis. The fracture properties of natural materials often outperform the fracture properties of artificial materials. An example of a natural material that outperforms artificial materials is nacre, which is shown on the front page of this report. During my master thesis I have studied the modulated effect of three different biomimetic design parameters, which are hard-soft material arrangement, hard material ratio and length scale, on the fracture properties of biomimetic hard-soft materials. This study shows that the fracture properties of hard-soft materials were mainly influenced by the length scale and hard material ratio. The fracture toughness of the hard-soft material samples could be increased by nearly two times compared to the toughness of the individual constituents, which supports the potential of biomimetic design parameters in increasing the fracture properties of hard-soft materials.

What I liked the most about my graduation project is that I got to learn a lot of new things, such as programming in R-code, performing tensile-tests, performing DIC measurements and taking images with a digital microscope. This would not have been possible without the help I received during my graduation. Therefore, I would like to thank everyone that was part of my graduation project. First of all, I would like to thank my supervisor Mohammad Mirzaali, who was really involved in the project. He always made time to help me, also via Skype when he was abroad. I enjoyed the meetings and discussions we had during my graduation. I would like to thank Amir Zadpoor for connecting me to this project within the Biomaterials and Tissue Biomechanics research group at the TU Delft and for his advice during the project. I would like to thank Zjenja Doubrovski of the Industrial Design faculty, who gave us the opportunity to work with the Objet500 Connex3 Polyjet printer during this project. He arranged the license required for using voxel-based AM. Zjenja also prepared the bitmap files required for voxel-based AM. I would like to thank Alba, who was doing her master internship about the same subject. We printed a lot of samples and performed a lot of tests together, which I enjoyed a lot. I would like to thank Gertjan Mulder of the Delft Aerospace Structures and Materials Laboratory for his help with the DIC measurements and tensile tests. I would like to thank Sander van Asperen, who gave me the instruction needed to use the digital microscope. The DIC measurements and digital microscope images were a great contribution to my graduation project and helped me with explaining the results. Furthermore, I would like to thank the members of my thesis committee for reading my report and attending my presentation. Last but not least, I would like to thank my family and friends, that supported me during graduation process, and during my study period as well.

Maike Edens
Delft, June 2018

Abstract

The fracture properties of natural materials often outperform artificial material properties. This could be explained by their complex multi-scale (anisotropic) hard-soft material structure, starting at a nano-scale. The interest in the fabrication of complex biomimetic hard-soft materials and interfaces is growing due to their high fracture properties. The high amount of stiffness, strength and fracture toughness present in natural composites is a desirable combination that is hard to obtain with conventional manufacturing techniques. Additive manufacturing, in particular voxel-based additive manufacturing, enables the precise mimicking of complex natural three-dimensional (3D) structures at a micro-scale. Various studies have been performed on the fabrication of biomimetic materials with an Objet500 Connex3 polyjet printer which is able to print multiple materials at the same time. However, fundamental research on the influence of multiple biomimetic design parameters on the fracture properties of hard-soft materials was missing. This research could contribute to improving the fracture properties of biomimetic materials.

In this study the isolated and modulated effects of three different biomimetic design parameters on the fracture properties of hard-soft material samples were analysed. The samples differed in length scale (40, 240, 480 and 960 μm), hard material ratio (0, 25, 38, 50, 63 75 and 100 %) and hard-soft material arrangement (semi-ordered, random and ordered). These design parameters could be found among different natural materials and interfaces. The fracture properties of the samples, including stiffness, fracture strength, final strain and fracture toughness, were obtained with a tensile test, in a similar way to previous literature studies. The effect of the different design parameters on the fracture properties was further analysed with digital image correlation (DIC) measurements and a digital microscope.

The results show that the biomimetic design parameters had a modulated effect on the fracture properties. The fracture properties were mostly affected by the hard material ratio and length scale compared to the hard-soft material arrangement. A higher amount of hard material resulted in a higher stiffness and fracture strength, but in a smaller final strain. A smaller length scale improved the fracture properties if a significant amount of soft material was present. Decreasing the length scale from 960 μm to 40 μm increased the fracture toughness by 1.7 to 5 times, depending on the hard material ratio and hard-soft material arrangement. Additionally, a decrease in length scale increased the stiffness by 0.89 to 9.7 times and the fracture strength by 1.4 to 3.6 times. An important result is that the fracture toughness of the hard-soft material samples could be increased by nearly two times compared to the toughness of the individual constituents, supporting the potential of using biomimetic design parameters. The effect of the biomimetic design parameters on the fracture properties can be explained by the DIC measurements and digital microscope images. The microscope images show that the fracture path tended to propagate through the soft material phases. Crack propagation through soft material was more difficult at a smaller length scale. DIC measurements showed that the plasticity zone in front of the crack tip was larger for the samples printed at native resolution, resulting in a higher fracture toughness. The hard-soft material arrangement and hard material ratio influenced the crack path and strain distributions especially at a higher length scale, explaining the greater difference in properties between the samples printed at a higher length scale.

This study shows that a wide range of fracture properties can be achieved by regulating the length scale, hard material ratio and hard-soft material arrangement of hard-soft materials. The fracture toughness of hard-soft materials can be improved in comparison to the fracture toughness of the individual constituents, which supports the potential of using biomimetic design parameters in improving the fracture properties of hard-soft materials.

Keywords: biomimetic materials; fracture properties; length scale; hard material ratio; hard-soft material arrangement; voxel-based additive manufacturing

Contents

List of Figures ix

List of Tables ix

1 Introduction 1
- 1.1 Research questions . . . 3
  - 1.1.1 Hypothesis . . . 4
- 1.2 Report structure . . . 4

2 Method 5
- 2.1 Objet500 Connex3 . . . 5
  - 2.1.1 Voxel-based additive manufacturing . . . 5
- 2.2 Fracture mechanics . . . 6
  - 2.2.1 Fracture properties . . . 8
- 2.3 Design parameters . . . 8
  - 2.3.1 Monolithic samples . . . 8
  - 2.3.2 Hard-soft material arrangement . . . 10
  - 2.3.3 Hard material ratio . . . 10
  - 2.3.4 Length scale . . . 10
- 2.4 Digital image correlation . . . 10
- 2.5 Digital microscope . . . 12

3 Results 15
- 3.1 Monolithic samples . . . 15
- 3.2 Hard material ratio . . . 15
- 3.3 Length scale . . . 16
- 3.4 Hard-soft material arrangement . . . 17
- 3.5 Modulated effect . . . 18
  - 3.5.1 Stiffness . . . 19
  - 3.5.2 Fracture stress . . . 21
  - 3.5.3 Final strain . . . 22
  - 3.5.4 Fracture toughness . . . 23
- 3.6 Digital image correlation . . . 24
  - 3.6.1 Semi-ordered . . . 24
- 3.7 Digital microscope . . . 26

4 Discussion 33
- 4.1 Monolithic samples . . . 33
- 4.2 Hard material ratio . . . 33
- 4.3 Length scale . . . 34
- 4.4 Hard-soft material arrangement . . . 35
- 4.5 Digital image correlation . . . 35
- 4.6 Digital microscope . . . 36
- 4.7 Comparison . . . 36
  - 4.7.1 Previous literature studies . . . 36
  - 4.7.2 Nature . . . 37
- 4.8 Limitations and recommendations . . . 38
- 4.9 Future research directions . . . 39

5 Conclusion **41**

Bibliography **43**

A Fracture properties **49**

B Digital image correlation images **51**

List of Figures

1.1 Different structures of natural materials 2

2.1 Schematic overview of the project 6
2.2 Binary images 7
2.3 Test set-up 7
2.4 Fracture properties 9
2.5 Hard-soft material arrangement 11
2.6 Length scale and hard material ratio 12
2.7 DIC test set-up 13

3.1 Monolithic samples 16
3.2 Effect hard material ratio 16
3.3 Effect length scale 17
3.4 Effect hard-soft material arrangement 18
3.5 Bar plots of the stiffness and the fracture stress for different length scales 19
3.6 Bar plots of the final strain and the fracture toughness for different length scales 20
3.7 Fracture toughness against the stiffness and fracture stress on a logarithmic scale . . . 21
3.8 Fracture properties of semi-ordered samples on a logarithmic scale 22
3.9 Rule of mixtures 23
3.10 DIC images of the ϵ_{yy} at highest applied force 25
3.11 DIC frames 26
3.12 DIC images of the semi-ordered samples with a hard material ratio of 75 %. 26
3.13 DIC images of the semi-ordered samples with a hard material ratio of 50 and 25 %. . . 27
3.14 Microscopy images monolithic samples 28
3.15 Microscopy images semi-ordered samples 29
3.16 Microscopy images random samples 30
3.17 Microscopy images ordered samples 31
3.18 Microscopy images of the semi-ordered samples for different length scales 32

4.1 Effect of biomimetic design parameters on fracture properties 34
4.2 Comparison with previous literature studies 37

B.1 DIC images of the ϵ_{xx} at highest applied force 52

List of Tables

2.1 Different hard-soft material samples 9

3.1 Fracture properties of monolithic samples 15
3.2 Effect of a decrease in length scale on fracture properties 23

A.1 Fracture properties of semi-ordered samples (75, 50 and 25 %) 49
A.2 Fracture properties of semi-ordered samples (62 and 38 %) 49
A.3 Fracture properties of random samples 50
A.4 Fracture properties of ordered samples 50

Nomenclature

Abbreviations

AM	=	additive manufacturing
DIC	=	digital image correlation
FDM	=	fused deposition modelling
FEM	=	finite element modelling
PLA	=	poly lactic acid
UV	=	ultraviolet
3D	=	three-dimensional

Symbols

a_0	=	initial crack length	mm
W	=	sample width	mm
L	=	sample length	mm
t	=	thickness	mm
b	=	strip length	mm
D	=	hole diameter	mm
σ	=	normal stress	MPa
F	=	applied load	N
A_0	=	effective cross section area	mm
ϵ	=	strain	$-$
E	=	stiffness	MPa
σ_f	=	fracture stress	MPa
ϵ_f	=	final strain	$-$
U	=	fracture toughness	MJ/m^3
ρ_h	=	hard material ratio	$\%$
E_h	=	hard material stiffness	MPa
E_s	=	soft material stiffness	MPa
ϵ_{yy}	=	strain distribution in the Y-direction	$-$
ϵ_{xx}	=	strain distribution in the X-direction	$-$

1 Introduction

Most artificial materials have either a high strength or high fracture toughness [1, 2]. A material with a high strength can withstand a high load before non-recoverable deformation or fracture occurs. However, materials with a high strength tend to be brittle when a crack initiates in the material, resulting in a low fracture toughness. In addition, ductile materials, which obtain a high plasticity zone, often have a low fracture strength. Both a high strength and high plasticity zone (high ductility) are required to obtain a high fracture toughness [1, 2]. A material with a high fracture toughness absorbs a high amount of energy before fracture [2].

Natural materials, which have been optimized to perform specific functions in their environment, outperform most man-made materials, due to their high strength and fracture toughness [2–12]. Examples of natural materials with a high strength and fracture toughness are: nacre, bone, wood, and biocalcite [1, 3, 4, 13, 14]. In addition, natural hard-soft material interfaces, such as the enthesis and osteochondral interface, are strong and tough compared to artificial bi-material interfaces [15, 16].

The high fracture properties of natural materials and interfaces can be explained by common characteristic natural design parameters [4]. First of all, natural materials are composed of hard and stiff building blocks which are bounded together with weaker material interfaces (Figure 1.1a) [4]. A natural material's high strength originates from the hard and stiff building blocks, which are inherently brittle. The weak interfaces enhance a material's toughness by inducing crack deflection and non-linear deformations [17, 18]. Furthermore, the high fracture properties of natural materials are related to their complex multi-scale (anisotropic) hierarchical architecture, starting at nano-scale (Figure 1.1b) [1, 3, 4, 13, 19–25]. The hierarchical hard-soft material arrangements at different length scales result in energy dissipation by intrinsic and extrinsic toughening mechanisms [1, 2, 4, 10, 14]. Intrinsic toughening mechanism act in front of a crack tip and at lower length scale (submicro-scale) compared to extrinsic toughening mechanisms, which act ahead of a crack tip and at micro- to macro scale [4]. The most important energy dissipation mechanisms in natural materials are: non-elastic deformation of soft organic material phases, crack blunting, crack branching, nucleation of micro-defects/micro-cracking, fibre bridging and fibre or platelet pull-out. [5, 6, 20, 21, 25–27].

There is a growing interest in the fabrication of complex biomimetic hard-soft materials and interfaces, due to their high fracture properties [4, 9–11, 30–46]. Various manufacturing techniques have been used to mimic hard-soft materials, including additive manufacturing (AM) [4, 8, 10, 16, 42, 45, 47–55], three-dimensional (3D) magnetic printing [56, 57], freeze casting and polymer infiltration [58–60], co-extrusion [61], layer-by-layer deposition [62–64], foaming [65, 66], laser engraving [67] and lamination [68]. AM can easily and rapidly mimic the complex hierarchical structure of natural materials, starting at micro-scale [8, 51–54, 69]. Generally, AM techniques build a structure by adding layers of cross-sections. The AM Polyjet technology is the only technology that is able to control both the layers and voxels at native print resolution [70]. Furthermore, Polyjet printers are able to drop a different material for each voxel, making voxel-based AM with a Polyjet printer a well-suited technique for the manufacturing of biomimetic hard-soft materials [3, 70].

Various studies have been performed on the fabrication of biomimetic materials with an Objet500 Connex3 Polyjet printer [3, 11, 37–40, 42–44, 47, 71, 72]. These studies show that it is possible to obtain a high fracture toughness with materials that are composed of hard and soft building blocks.

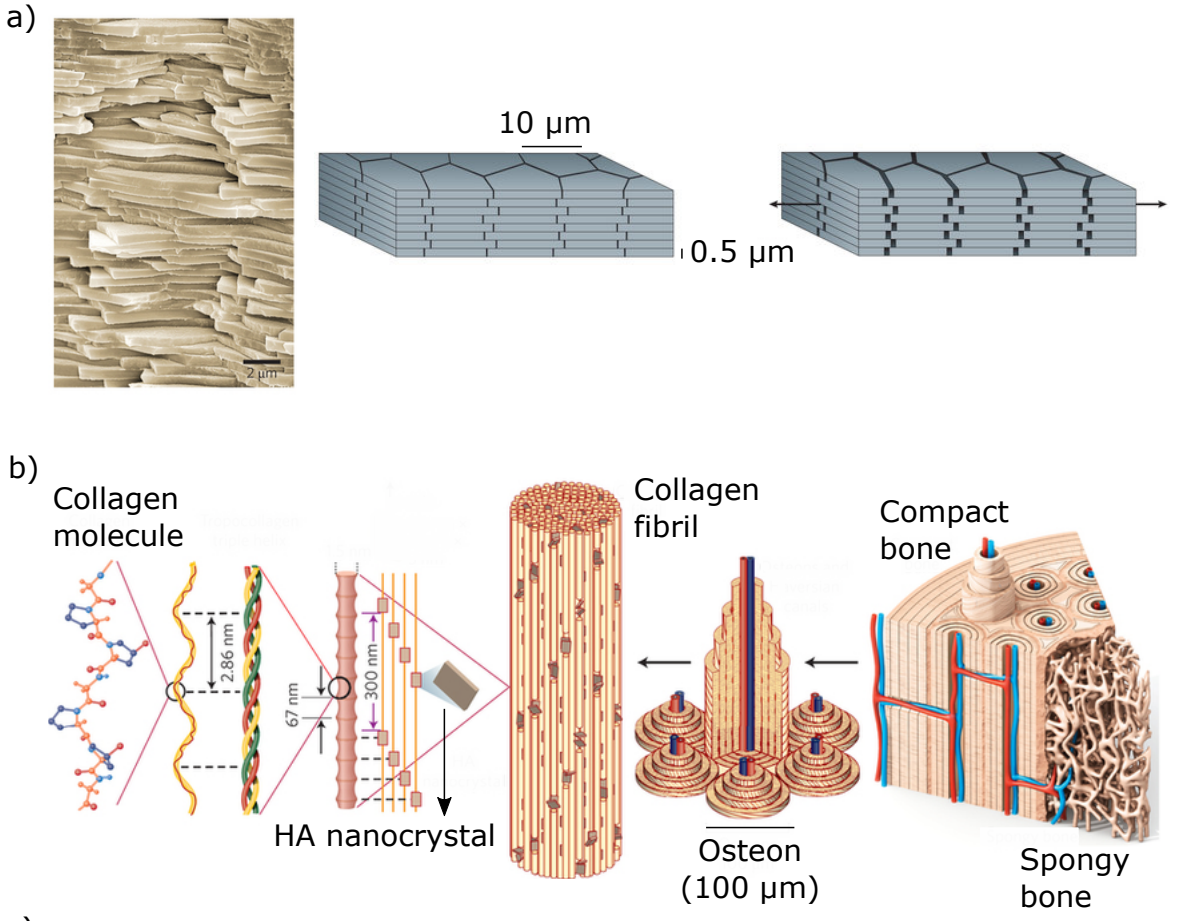


Figure 1.1: Different structures of natural hard-soft materials. a) The typical brick and mortar structure of nacre at micro-scale [10, 18]. b) The hierarchical structure of bone at different length scales [10]. c) The graded structure of the enthesis [28, 29].

Different hard-soft material arrangements have been studied, including bone-like / brick-and-mortar [11, 34–37, 44], rotated bone-like [11, 35, 36], biocalcite-like [11, 34–36], haversian [47], topological interlocked [40, 43] and algorithm-based structures [41, 72]. However, the fracture behaviour of these structures was highly dependent on the loading angle [44]. Additional studies show that fracture behaviour of biomimetic hard-soft composites was influenced by different design parameters, including the amount of hierarchical levels [34, 39], voxel-length [71], initial crack length [39], stiffness ratio [37], and the volume fraction of hard material [42]. These design parameters influenced the crack path propagation and the amount of stress and strain localization [34, 37, 39, 42, 71]. The previous mentioned studies show the potential of manufacturing biomimetic designed structures with an Objet500 Connex3 printer. However, the analysis of biomimetic materials with a Objet500 Connex3 printer is

limited. Fundamental research on the effect of multiple biomimetic design parameters on the strength and fracture toughness of hard-soft materials is missing. This research could contribute to improving the fracture properties of biomimetic materials.

In this work, the effect of length scale, hard material ratio and hard-soft material arrangement on the fracture properties of biomimetic hard-soft materials is analysed. These design parameters could be found among different natural materials and interfaces. First of all, natural materials show complex structures at different length scales (Figure 1.1b). The effect of length scale on the fracture properties has not been studied before. Furthermore, the effect of printing hard and soft building blocks at native print resolution has not been studied. Secondly, natural materials differ in hard material ratio. The ratio of hydroxyapatite in bone is equal to approximately 60 % [73], whereas in nacre, the ratio of hard aragonite bricks is equal to 95 % [5, 74]. Besides the difference in hard material ratio, natural materials are organized in different ways, depending on their environment and on the required properties. The hard-soft material arrangement of natural materials varies between ordered to randomized structures. An example of an ordered structure is the typical brick-and-mortar structure that can be found in nacre (Figure 1.1a) [5, 75]. More randomized arrangements can be found at the enthesis and osteochondral interface, which both show a random distribution in mineral content and collagen orientation (Figure 1.1c) [76]. In this study, the hard-soft material arrangement is regulated by three different algorithms, which are semi-ordered, random and ordered. The hard-soft material arrangement is distributed in all directions, resulting in a heterogeneous arrangement of hard and soft material phases in all directions [32]. This differs from previous studies, which were limited to transversely isotropic arrangements [3, 11, 37–40, 42–44, 47, 72]. Voxel-based AM gives the opportunity to quickly design and manufacture different complex hard-soft material samples which vary in length scale, hard material ratio and hard-soft material arrangement. The isolated and modulated effects of these biomimetic design parameters on the fracture properties, including stiffness, fracture stress, final strain and fracture toughness, is analysed in this study.

1.1. Research questions

The main research question of this study is:

- **What are the isolated and modulated effects of the biomimetic design parameters, including length scale, hard material ratio and hard-soft material arrangement, on the fracture properties of biomimetic hard-soft materials?**

The main research question is divided in different sub-questions. Firstly, the isolated effect of the three different biomimetic design parameters on the stress-strain curve is studied, resulting in the following sub-questions:

- **What is the effect of length scale on the stress-strain curve?**
- **What is the effect of hard material ratio on the stress-strain curve?**
- **What is the effect of hard-soft material arrangement on the stress-strain curve?**

The effect of the biomimetic design parameters on the fracture properties can be derived from the stress-strain curves. Besides the isolated effect, the design parameters could influence the fracture properties in a modulated way. The modulated effect of the different design parameters on the fracture properties is captured in the following sub-questions:

- **What is the modulated effect of the biomimetic design parameters on the stiffness?**
- **What is the modulated effect of the biomimetic design parameters on the fracture stress?**
- **What is the modulated effect of the biomimetic design parameters on the final strain?**
- **What is the modulated effect of the biomimetic design parameters on the fracture toughness?**

The modulated effect of the biomimetic design parameters on fracture properties can be further explained by their effect on the fracture behaviour of the samples. The fracture behaviour is studied with digital image correlation (DIC) measurements and a digital microscope. DIC measurements show the influence of the biomimetic design parameters on the strain distributions. The influence of the biomimetic design parameters on the crack path is studied using a digital microscope. The main research questions can be answered based on the seven sub-questions and the fracture behaviour of the different samples.

1.1.1. Hypothesis

The hypothesis is that all three biomimetic design parameters affect the fracture properties and fracture behaviour of the samples. First of all, a smaller length scale results in high fracture properties. Secondly, the hard material ratio affect the properties in different ways. A higher hard material ratio results in a higher stiffness and fracture stress, whereas a smaller ratio results in a higher final strain. A sufficient amount of hard and soft material phases is required to obtain a high fracture toughness. The hypothesis is that the fracture toughness of the hard-soft material samples is improved compared to the fracture toughness of the individual constituents. Lastly, the hard-soft material arrangement affects the fracture properties by influencing the fracture path, which tends to propagate through soft material phases [11]. The biomimetic design parameters have a modulated effect on the fracture properties, which means that the effect of a design parameter on the properties is influenced by the other two design parameters. For example, the effect of length scale on the fracture properties is affected by the hard material ratio and hard-soft material arrangement.

1.2. Report structure

The report is organized as follows; the next chapter describes the different methods that are used. The results are given in Chapter 3, in which also the seven sub-questions are answered. Chapter 4 (Discussion) discusses the results and the accuracy and the limitations of this study. The discussion closes with recommendations for further research directions. The report ends with a conclusion (Chapter 5), in which the main research question is answered.

2
Method

Figure 2.1 shows a schematic overview of the project, which is about the effect of biomimetic design parameters on fracture properties. The biomimetic design parameters analysed in this study were based on the different structures of natural materials. The hard-soft material samples varied in hard-soft material arrangement, hard-material ratio and length scale. Voxel-based AM with an Objet500 Connex3 printer was used to manufacture the samples. The printer is explained in the first part of this chapter. The geometry of the samples was similar to previous literature studies [11, 37, 39, 40, 42, 47, 72]. Furthermore, a tensile test was used to measure the fracture properties, in a similar way to previous literature studies [11, 37, 39, 40, 42, 47, 72]. The effect of biomimetic design parameters on the fracture properties, including stiffness, fracture stress, final strain and fracture toughness, was studied. The fracture behaviour of the samples was more comprehensively studied with DIC measurements (2.4), which showed the effect of biomimetic design parameters on the strain distribution, and a digital microscope (2.5), which showed the effect of biomimetic design parameters on the fracture path.

2.1. Objet500 Connex3

The samples were printed with an Objet500 Connex3 3D printer, which is a Polyjet printer that can print multiple materials at the same time. The printer has two base materials: rigid (Vero) material and flexible (Tangoplus) material, which are both acrylic-based photopolymers [47]. These materials have contradicting properties which is caused by a difference in the amount of cross-links between polymer chains. Vero materials have a high tensile strength and a small elongation at break, whereas Tango materials, which show elastomeric characteristics, have a low tensile strength and a high elongation at break [79]. The printer contains eight printing heads, of which six heads can be used in pairs to print three different materials and of which two heads print support material. Therefore, the Objet500 Connex3 printer can deposit three different materials and one support material at the same time. The materials, which are located in cartridges, are connected to the printing heads by a liquid system. One printing head contains numerous aligned nozzles, that jet material droplets on the building tray, which moves down during printing. The droplets, which are composed of oligomers, monomers and photo-initiators, are directly cured with ultraviolet (UV) light, that solidifies the printed droplets. Direct solidification allows continuous printing of new layers and guarantees a good adhesion between the hard and soft material phases. The printing position on the building tray influences the material properties [80]. All samples were printed one after another at the same position on the building tray to prevent this effect. Furthermore, all samples were printed in the same orientation [80]. The support material was removed after printing. Subsequently, the samples were cleaned carefully with ethanol.

2.1.1. Voxel-based additive manufacturing

The samples were printed using voxel-based AM. This technique gives the possibility to control material deposition at native print resolution, which is not possible by using STL files [81]. The resolution of the printer is 600 dpi (X-axis), by 300 dpi (Y-axis), by 847 dpi (Z-axis), resulting in a minimal voxel size of 42*84*30 μm. A voxel, which is known as a volumetric pixel, is a volume element on a regular grid in a 3D space. A model should be sliced in different layers with a thickness of 30 μm, which is the voxel

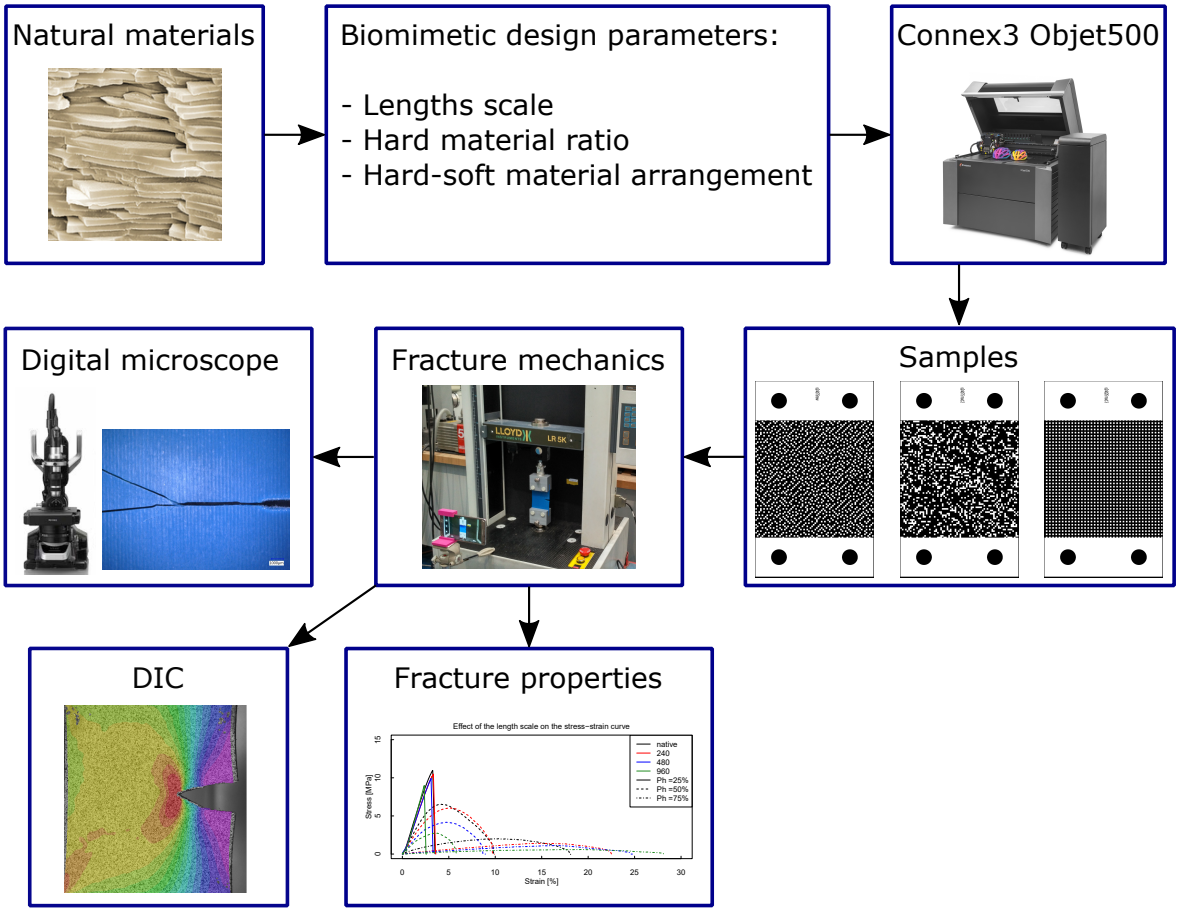


Figure 2.1: Schematic overview of the project. The biomimetic design parameters were selected based on the different structures of natural materials [10]. The samples were manufactured by using an Objet500 Connex3 printer [77]. A tensile test was used to measure the fracture properties. The fracture behaviour was more comprehensively studied with DIC measurements and a digital microscope [78].

length in the Z-direction, for voxel-based AM. The total number of slices equals the sample thickness divided by the thickness of one layer (30 μm). Our sample thickness was equal to 3 mm, consequently 100 layers were required. A bitmap file is required for each layer and every material of the printer. A bitmap file is known as a binary image in which each pixel has two possible values: 0 or 1. A material is printed in the layer if the pixel in the binary image has value of 1. In other words, a white pixel, which has a value of 1, means that the material will be deposited at that position. The bitmaps of different materials could not overlap, because it is not possible to print more than one material at the same voxel. Figure 2.2 shows the binary images of three different materials (A, B and C) for one layer. The right image shows the outcome of these bitmap files.

2.2. Fracture mechanics

The material fracture properties could not be obtained with ASTM test procedures (CT and SENB), because the materials did not met the standards of these procedures [82]. The sample dimensions and test set-up used in this study are comparable to previous literature studies, in which the fracture properties of single edge notched samples were measured using a tensile test method (Figure 2.3) [11, 37, 39, 40, 42, 47, 72]. Figure 2.3a shows the sample dimensions. The crack was printed within the sample. The initial crack length (a_0) was equal to 15 mm, which was 20 % of the sample width (W = 75 mm). The sample width was similar to the sample length (L). The samples had a thickness of 3 mm. A hard Vero material strip was printed at the upper and lower part of the samples. The strips, which had a length (b) of 25 mm and width (W) of 75 mm, contained two holes with a diameter

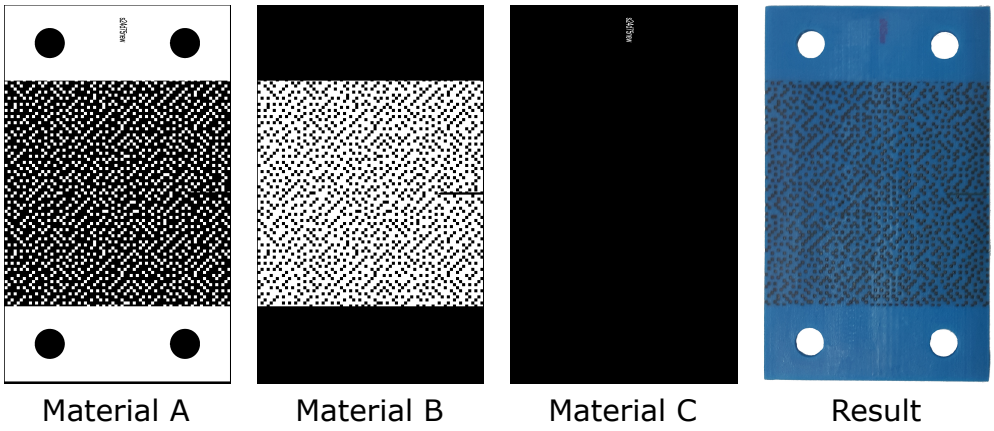
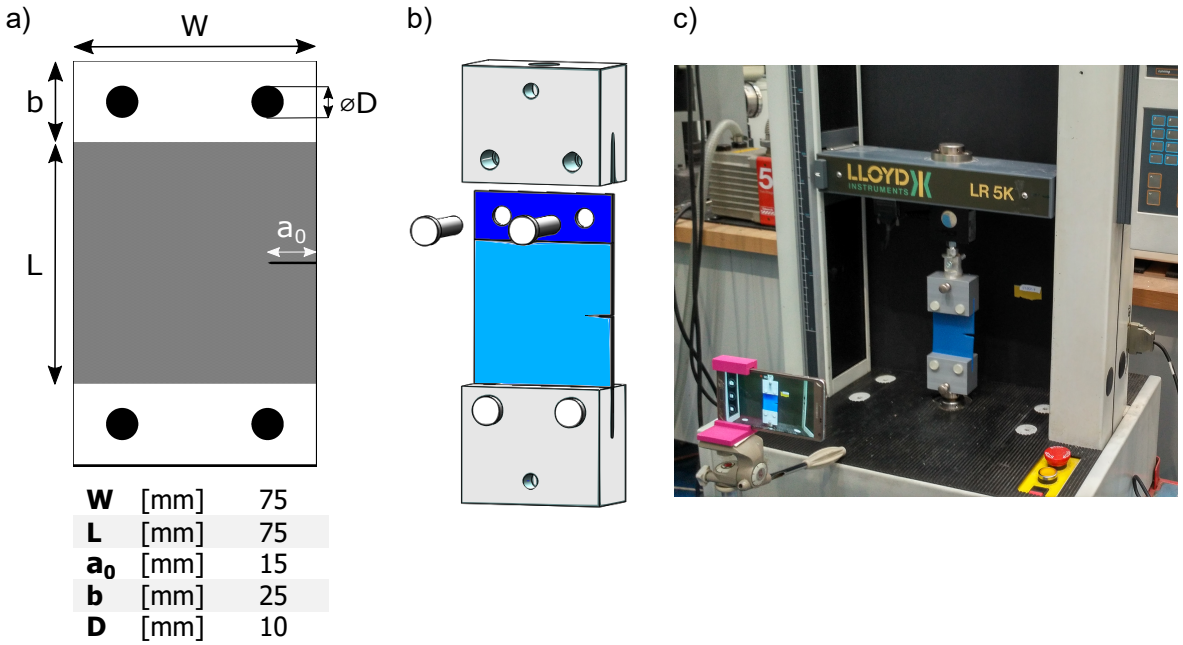


Figure 2.2: Binary images of three different materials (A, B and C) for one layer. A material is deposit for every white pixel. The right images shows the result of the three binary images.



W	[mm]	75
L	[mm]	75
a_0	[mm]	15
b	[mm]	25
D	[mm]	10

Figure 2.3: a) The dimensions of the samples with a single edge notch are given in the table. b) The upper and lower strip of the samples were attached to the grippers by four pins. c) The complete tensile test set-up. The grippers were attached to the Lloyd tensile test machine. All samples were filmed during testing.

(D) of 10 mm. The strips were used to fixate the sample via two holders and four pins to the tensile test machine (Figure 2.3b and c). The holders and pins were manufactured using a fused deposition modelling (FDM) 3D printer (Ultimaker 2+, Geldermalsen, the Netherlands) with polyactic acid (PLA) filaments (MakerPoint PLA 750 gr Natural). The complete hard samples were tested with an aluminium gripping system (holders and pins) that had the same dimensions. All the samples were filmed during testing. The fracture tests were performed on a LLOYD tensile test machine (Figure 2.3c). A 5 kN load cell was used to measure the load that was required to deform the samples with a displacement rate of 2 mm/min. 5 kN is higher than the maximum load that was required to fracture the samples. The pre-load was equal to 1 N according to the loading protocol. The lower strip of the samples stayed in position while the displacement rate of 2 mm/min was applied on the upper strip of the samples. Samples were loaded until complete fracture. All samples were placed with the initial crack at the right side and the strip with the name tag at the upper side, The time, load, extension, and deflection from

pre-load were obtained at a frequency of 20 Hz during testing. The data was divided in 200 data points after testing. The fracture properties were derived from these data points using RStudio (RStudio, Inc., Boston, MA, 2015).

2.2.1. Fracture properties

The stress-strain curves were derived from the load and extension values, in the following way:

- Normal stress (σ) in MPa : The normal stress was defined as the ratio of applied load (F) to the effective cross section area (A_0):
$$\sigma = F/A_0 \tag{2.1}$$
In which the effective cross section area equals:
$$A_0 = t * (W - a_0) \tag{2.2}$$
In which t = thickness, W = width and a_0 = initial crack length (Figure 2.3).
- Strain (ϵ) : The strain was defined as the ratio of extension to the initial sample length ($L = 75mm$):
$$\epsilon = \Delta L/L \tag{2.3}$$

The effect of biomimetic design parameters on the fracture properties, which are stiffness, fracture stress, final strain and fracture toughness, was studied. These fracture properties can be derived from the stress-strain curve (Figure 2.4) The fracture properties are described in more detail below:

- Stiffness (E) in MPa : The stiffness was defined as the stiffest slope of the elastic part of the stress-strain curve. The stiffest slope was calculated using a moving regression algorithm, in which only the first 1 % of the strain was included.
- Fracture stress (σ_f) in MPa : The fracture stress was defined as the maximum obtained stress.
- Final strain (ϵ_f) in $\%$: The final strain was defined as the maximum obtained strain.
- Fracture toughness (U) in MJ/m^3: The fracture toughness was defined as the area under stress-strain curve, which was obtained by using numerical integration.
$$U = \int_0^{\epsilon_f} \sigma_f \, d\epsilon \tag{2.4}$$

Equation 2.4 shows that both a high fracture stress and final strain were required to obtain a high fracture toughness.

2.3. Design parameters

The hard-soft material samples were composed of two materials with highly contrasting properties: hard Vero and soft Tango material. The effect of the biomimetic design parameters, which are hard-soft material arrangement, hard material ratio and length-scale, on fracture properties was studied by 46 different designs. Table 2.1 gives an overview these different designs. The first arrangement, which is the semi-ordered arrangement, was studied for four different length scales (40, 240, 480 and 960 μm) and five different hard material ratios (25, 38, 50, 62 and 75 %), resulting in 20 different designs (Table 2.1a and 2.1b). In addition, four different length scales (40, 240, 480 and 960 μm) and three different hard material ratios (25, 50 and 75 %) were studied for a random and ordered arrangement, resulting in 24 different designs (Table 2.1c and 2.1d). Furthermore, complete soft and hard samples were tested. Every design was printed and tested three times, resulting in 138 different tests. The samples were printed in different colours, which was dependent on the available colours in the printer at the moment of printing.

2.3.1. Monolithic samples

The individual fracture properties of the two building blocks were obtained with the monolithic samples. The hard material ratio was equal to 100 for a complete hard material and 0 for a complete soft material. The monolithic samples were printed at native resolution.

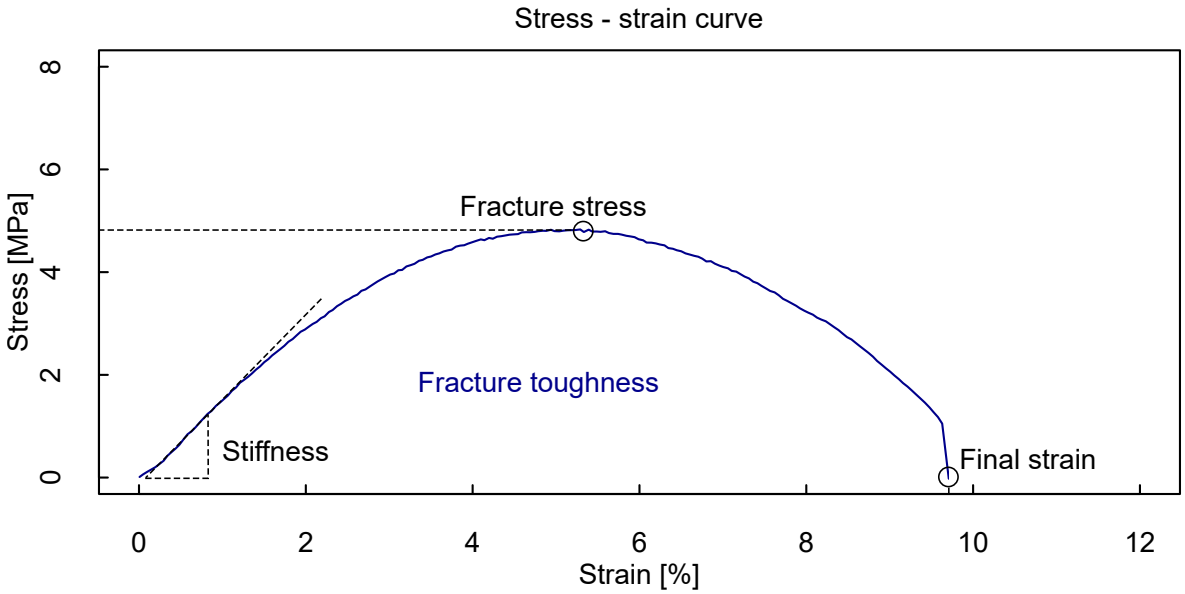


Figure 2.4: The fracture properties, including stiffness, fracture stress, final strain and fracture toughness, can be derived from the stress-strain curve. The stiffness is equal to the stiffest slope of the elastic part of the stress-strain curve. The fracture stress is equal to the maximum obtained stress. The final strain is defined as the maximum obtained strain. Lastly, the fracture toughness is defined as the area under the stress-strain curve.

Table 2.1: The different hard-soft material samples. The samples in bold were analysed with DIC measurements. In addition, the samples in italic were analysed with a digital microscope.

(a) The semi-ordered samples with a hard material ratio of 75, 50 and 25 %.

	Semi-ordered											
ρ_h [%]	75				50				25			
Length scale [μm]	***40***	240	480	***960***	***40***	240	480	***960***	***40***	*240*	*480*	***960***

(b) The semi-ordered samples with a hard material ratio of 62 and 38 %.

	Semi-ordered							
ρ_h [%]	62				38			
Length scale [μm]	40	240	480	960	40	240	480	960

(c) The random arranged samples with a hard material ratio of 75, 50 and 25 %.

	Random											
ρ_h [%]	75				50				25			
Length scale [μm]	***40***	240	480	***960***	***40***	240	480	***960***	***40***	240	480	***960***

(d) The ordered samples with a hard material ratio of 75, 50 and 25 %.

	Ordered											
ρ_h [%]	75				50				25			
Length scale [μm]	***40***	240	480	***960***	***40***	240	480	***960***	***40***	240	480	***960***

2.3.2. Hard-soft material arrangement

Three different hard-soft material arrangements were studied to obtain the influence of hard-soft material organization on the fracture properties and fracture behaviour. The arrangements were obtained using computer algorithms. An algorithm made the voxel-length and hard-soft material ratio easily adjustable. An error diffusion, random and ordered dither algorithm were used to obtain respectively a semi-ordered, random and ordered hard-soft material arrangement. The three different algorithms are discussed below:

1. **Error diffusion:** The first arrangement was constructed using an error diffusion algorithm. In an error diffusion algorithm influences the value of a voxel, which can be hard or soft, the values of its adjacent voxels. Different coefficients can be used to propagate the value of a voxel to its neighbours. The Floyd-Steinberg algorithm was used to construct the error-diffusion arrangement in this study [83]. The error diffusion algorithm resulted in a semi-ordered hard-soft material arrangement.

2. **Random:** The second arrangement was constructed with a random algorithm. The hard and soft voxels were randomly distributed through the material. The only constraint was the hard material ratio, which had to be the same for every layer.

3. **Ordered dither:** The third arrangement was constructed with an ordered dither algorithm. A volume dithering pattern was required to avoid that the arrangement would look exactly the same in every layer [84]. Four different matrices were used to obtain a 4x4x4 pattern. A voxel was composed of soft material if the value in the matrix was equal to or higher than the threshold value, which was dependent on the hard material ratio. The volume dithering algorithm did not result in the same hard material ratio for every layer, yet the overall hard material ratio of the samples was equal to the required ratio.

The error diffusion and ordered dither algorithms resulted in the same arrangement for the samples with an equal amount of hard and soft material. Figure 2.5 shows the different arrangements for three different hard material ratios at the highest length scale.

2.3.3. Hard material ratio

The samples differed in hard material ratio (ρ_h). Samples with a hard material ratio of $\rho_h = 25\%$, $\rho_h = 50\%$ and $\rho_h = 75\%$ were tested for all three hard-soft material arrangements. Additionally, samples with a ratio of $\rho_h = 38\%$ and $\rho_h = 62\%$ were tested for the semi-ordered samples. Figure 2.6 shows the effect of hard material ratio on the samples with a semi-ordered arrangement. The positions of the hard material voxels of the $\rho_h = 75\%$ samples were equal to positions of the soft material voxels of the $\rho_h = 25\%$ samples. Similarly, the positions of the hard material voxels of the $\rho_h = 62\%$ samples were equal to the positions of the soft material voxels of the $\rho_h = 38\%$ samples.

2.3.4. Length scale

In addition to the hard-soft material arrangement and hard material ratio, the samples differed in length scale. The effect of length scale was studied by a difference in voxel length. Figure 2.6 shows the effect length scale on the binary images of the semi-ordered samples. Four different voxel-lengths were analysed, including native resolution, 240 μm, 480 μm and 960 μm. The native resolution of the Connex500 Objet3 is 600 dpi (X-axis), by 300 dpi (Y-axis), by 847 dpi (Z-axis), which results in a minimal voxel size of 42*84*30 μm. A voxel length of 40 μm refers to the native resolution in the remaining of this report. The voxels with a length scale of 240 μm, 480 μm and 960 μm were cubic.

2.4. Digital image correlation

DIC was used to measure the strain distributions in the X- and Y-direction. Figure 2.7a shows the DIC test set-up, which is comparable to the test set-up described in Section 2.2. The DIC tensile tests were performed on a Zwick Roell machine (Zwick GmbH & Co. KG) using a displacement rate of 2 mm/min. A 20 kN load cell was used to measure the load. The front surfaces of the samples were sprayed white and afterwards covered with randomly sprayed black speckles (Figure 2.7b). The samples were lightened (Profilux LED) during testing to increase the contrast between white and black

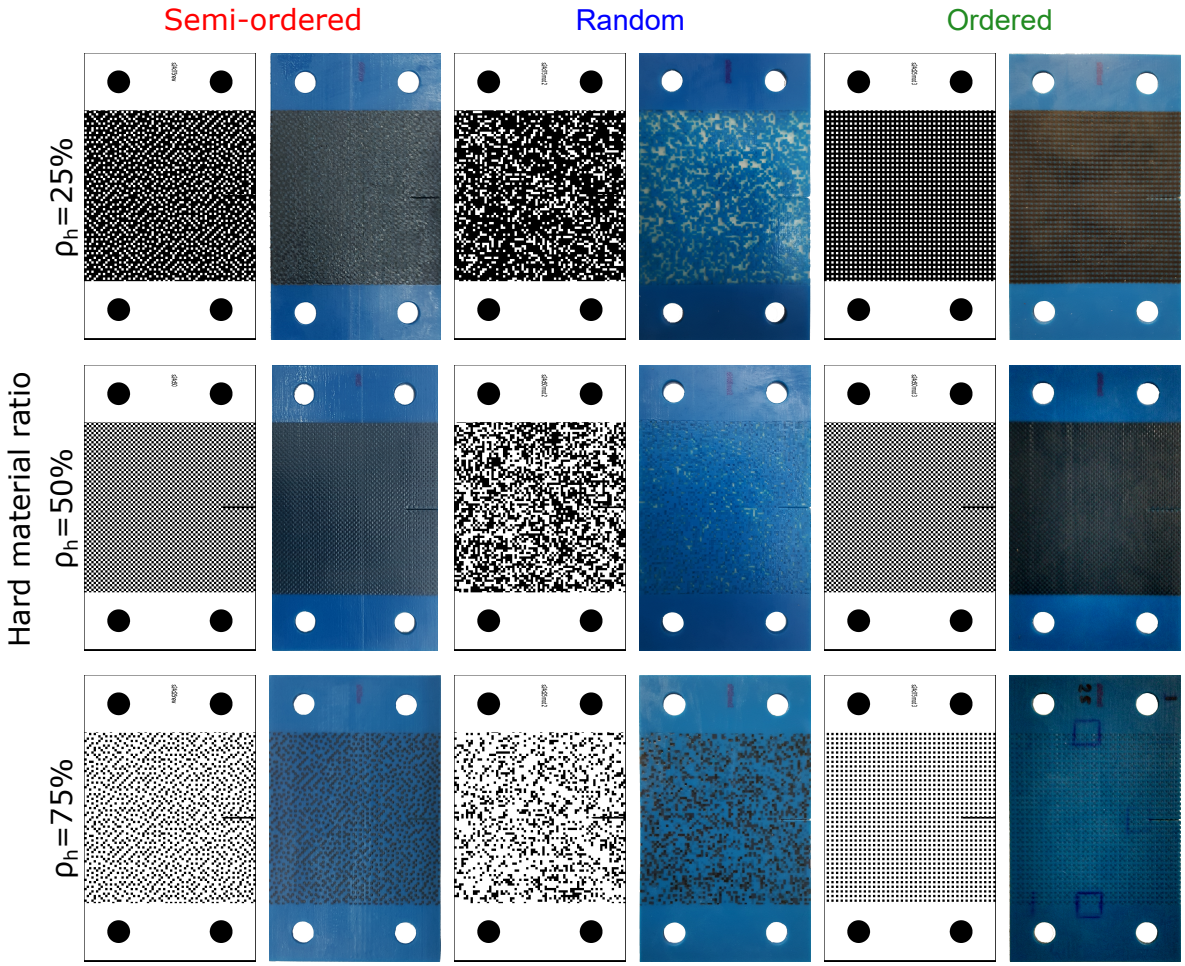


Figure 2.5: Images of the different hard-soft material arrangements, which are semi-random, random and ordered. The material arrangements are shown for three different hard material ratios at the highest length scale

dots. The two cameras (4MP cameras with CMOS chip), which were placed in front of the test set-up, were connected to the computer. The cameras were calibrated before testing to obtain the positions and angles of the cameras with respect to each other. The calibration value was equal to 0.035 in this study. One image was taken every second during testing. The Vic-3D software (Vic-3D 8, Correlated Solutions, SC, USA) was used to derive the strain distributions from the displacements of the white and black dots. A subset of 29 and a step size of 7 were used to calculate the strain distributions.

Two strain components were analysed in this study: ϵ_{xx} and ϵ_{yy}. ϵ_{yy} was defined as the strain in the longitudinal direction, which was the direction of applied load, whereas ϵ_{xx} was defined as the strain in the perpendicular direction (Figure 2.7b). DIC measurements were performed for different samples to obtain the effect of the biomimetic design parameters on the stress distributions. Measurements were performed once for the samples with a voxel length of 40 and 960 μm for all three arrangements and for a hard material ratio of $\rho_h = 25\%$, $\rho_h = 50\%$ and $\rho_h = 75\%$. This is shown by the bold samples in Table 2.1. The ϵ_{xx} and ϵ_{yy} distributions at the frame of highest applied load were analysed for all samples. These frames showed the effect of hard-soft material arrangement on the strain distributions in both directions. Additionally, the ϵ_{yy} distribution of the semi-ordered samples was analysed at five different frames, which were the initial frame, the frame at highest force and three frames in between for the $\rho_h = 75\%$ samples. The initial frame, the frame at highest force, one frame before fracture and two frames in between were studied for the $\rho_h = 25\%$ and $\rho_h = 50\%$ samples. These frames showed the effect of hard-material ratio and length scale on the ϵ_{yy} distribution.

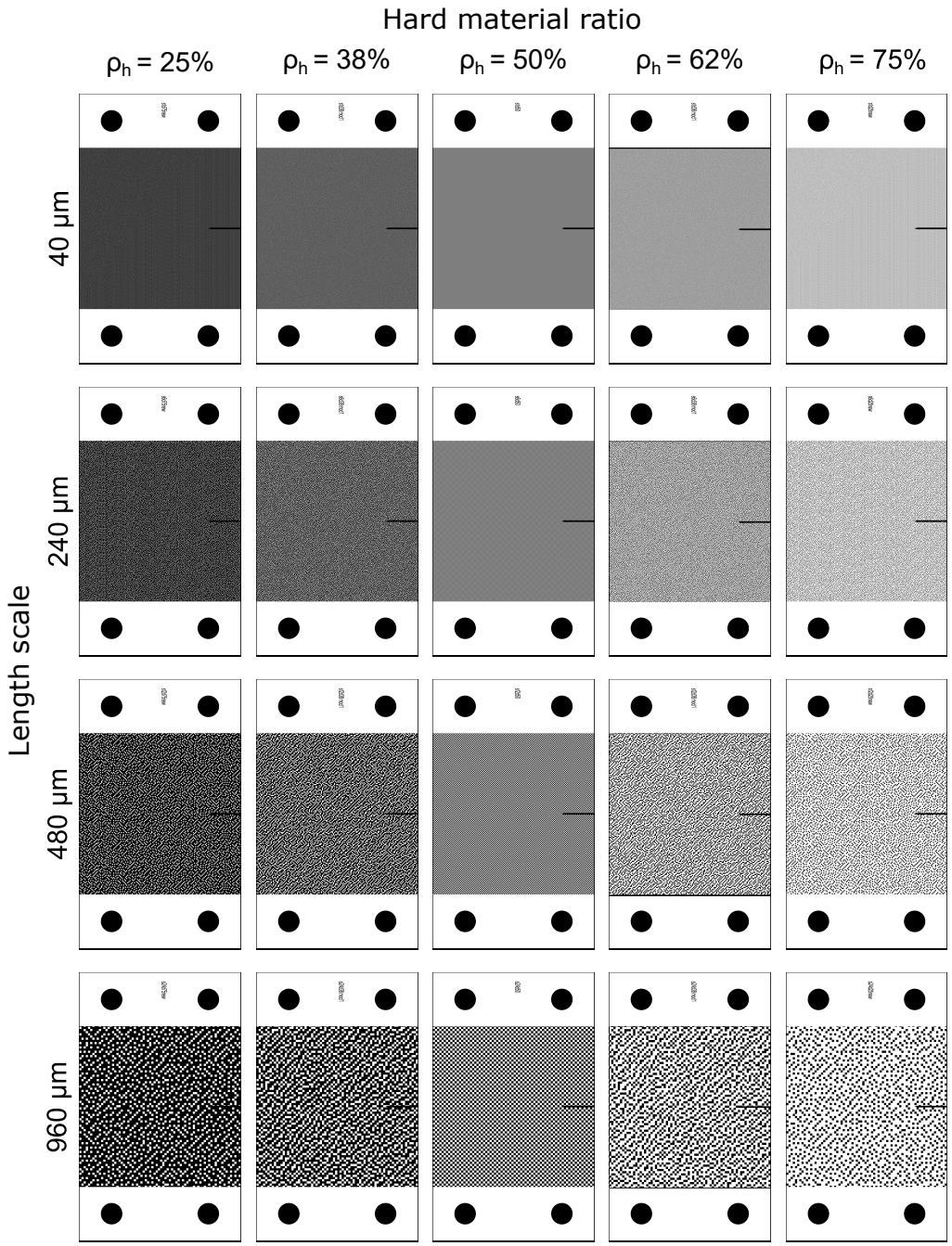


Figure 2.6: Binary images of semi-ordered samples for five different hard material ratios (25, 38, 50, 62 and 75 %) and four different length scales (40, 240, 480 and 960 μm).

2.5. Digital microscope

The fracture path of different samples were studied by using a Keyence digital microscope (Keyence VHX-5000) with a VH-Z20T lens using a 20x and 200x magnification. The stitch image function was used to capture a wider range of the fracture paths. The crack path of different samples, which are shown in italic in Table 2.1, was studied to obtain the influence of the biomimetic design parameters on crack propagation. The fracture path of the semi-ordered samples was analysed for all four length scales and a hard material ratio of $\rho_h = 25\%$, $\rho_h = 50\%$ and $\rho_h = 75\%$. The top view of the crack interface was also studied for these samples. These samples were studied to obtain the effect of hard material ratio and length scale on the fracture path. Additionally, the fracture path of the random

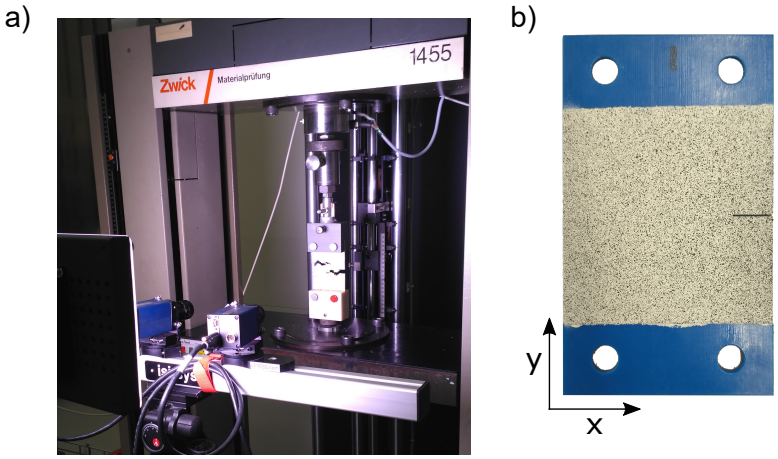


Figure 2.7: a) The DIC tensile test set-up, including a speckled sample that was fixated to the Zwick tensile test machine with the pins and holders, two cameras and the LED lamp. b) A speckled sample with the indicated X- and Y-direction.

and ordered samples with a voxel length of 40 and 960 μm was analysed for a hard material ratio of $\rho_h = 25\%$, $\rho_h = 50\%$ and $\rho_h = 75\%$. These samples were studied to obtain the effect of hard-soft material arrangement on the fracture path.

3

Results

This chapter describes the fracture properties and fracture behaviour of the different samples. At first, the fracture mechanics of the monolithic samples are described. Subsequently, the effect of the biomimetic design parameters, which are hard material ratio, length scale and hard-soft material arrangement, on the stress-strain curve is described. Additionally, the modulated effect of the biomimetic design parameters on the fracture properties is reported. The fracture properties described in this chapter were derived from the stress-strain curves. Appendix A gives the mean values and standard deviations of the fracture properties for all length scales, hard material ratios and hard-soft material arrangements. This chapter closes with a description of the DIC measurements and digital microscope images.

3.1. Monolithic samples

Figure 3.1 shows the stress-strain curves of the monolithic hard and soft samples. The hard (Vero) material samples fractured at a high stress and a low strain, whereas the soft (Tangoplus) samples fractured at a low stress and a high strain (Table 3.1). In addition, Table 3.1 shows that the hard samples obtained a higher fracture toughness compared to the soft samples. The monolithic materials showed different fracture mechanisms. The hard samples showed an almost linear stress-strain curve. These samples fractured abruptly and in a brittle way. The fracture path of all hard samples branched during fracture. The soft samples, which fractured in a ductile way, showed crack blunting during fracture. Furthermore, the stress-strain behaviour of the soft materials was non-linear (Figure 3.1). To conclude the monolithic samples showed contradicting fracture properties and fracture behaviours.

Table 3.1: The fracture properties of the monolithic samples. The mean value and standard deviation are given.

Monolithic Sample	E $[MPa]$	σ_f $[MPa]$	ϵ_f $[\%]$	U $[MJ/m^3]$
ρ_h = 0 $\%$	0.803 ± 0.059	0.203 ± 0.014	35.5 ± 3.5	0.041 ± 0.0065
ρ_h = 100 $\%$	740 ± 27	15.4 ± 1.3	3.35 ± 0.32	0.216 ± 0.058

3.2. Hard material ratio

Figure 3.2 shows the effect of hard material ratio on the stress-strain curve for one hard-soft material arrangement (semi-ordered) and one voxel-length (960 μm). The figure shows that a higher amount of hard material resulted in a higher fracture stress, whereas a higher amount of soft material resulted in a higher final strain. The hard material ratio influenced the fracture behaviour of the samples. All $\rho_h = 62\%$ and $\rho_h = 75\%$ samples fractured in a brittle way. These samples showed a linear stress-strain curve. 36 samples with a hard material ratio of 75 % were tested, of which 31 samples showed crack branching. Five $\rho_h = 75\%$ samples with a voxel-length of 960 μm did not show crack branching, including the three random organized samples. 9 of the 12 samples with a hard material ratio of 62 % showed crack branching. The three $\rho_h = 62\%$ samples with a voxel-length of 960 μm did not show crack branching. All $\rho_h = 50\%$, $\rho_h = 38\%$ and $\rho_h = 25\%$ samples fractured in a ductile way.

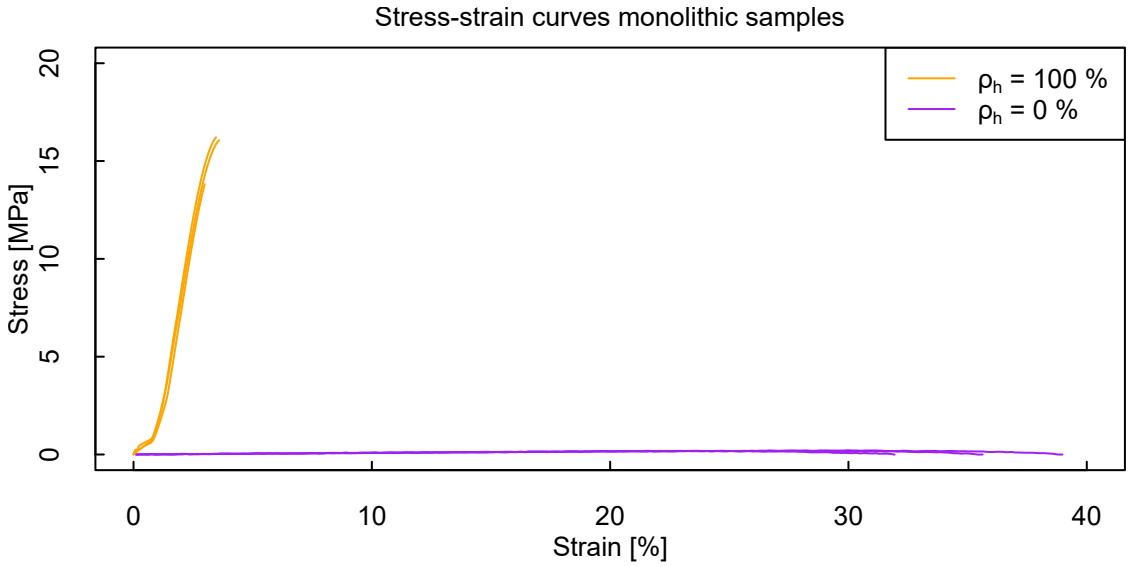


Figure 3.1: a) The stress-strain curves of the monolithic samples. The three hard samples ($\rho_h = 100\%$) fractured at a high stress and a low strain, whereas the three soft samples ($\rho_h = 0\%$) fractured at a low stress and a high strain.

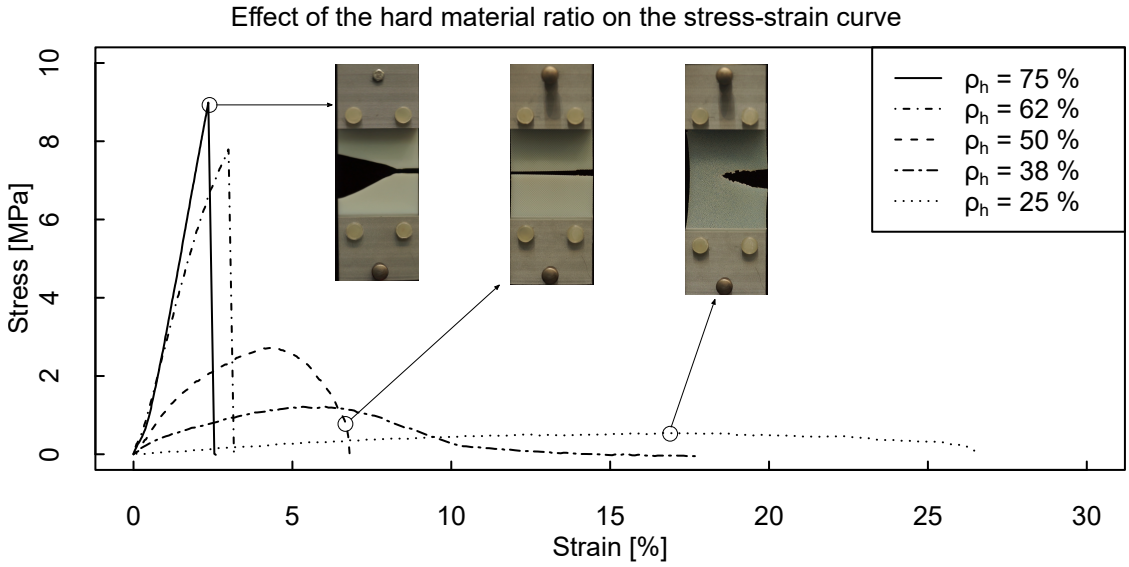


Figure 3.2: The stress-strain curves of semi-ordered samples with a voxel length of 960 μm, that were tested as third. The graph shows the effect of hard material ratio on the stress-strain curve. Additionally, the fracture paths of the $\rho_h = 75\%$, $\rho_h = 50\%$ and $\rho_h = 25\%$ samples are shown.

Figure 3.2 shows that the stress-strain curves of these samples are non-linear. Furthermore, these samples showed crack blunting during fracture. The amount of crack blunting was dependent on the hard material ratio. A higher amount of soft material resulted in more crack blunting. To summarize, the hard material ratio affected the stress-strain curves and fracture behaviours of the samples. The $\rho_h = 75\%$ and $\rho_h = 62\%$ samples showed crack branching and fractured in a brittle way, whereas the $\rho_h = 50\%$, $\rho_h = 38\%$ and $\rho_h = 25\%$ samplesj showed crack blunting and fractured in a ductile way.

3.3. Length scale

Figure 3.3 shows the effect of length scale on the stress-strain curves of the semi-ordered samples for three different hard material ratios (75, 50 and 25 %). The length scale affected the stress-strain curve in different ways. Firstly, the $\rho_h = 75\%$ samples were less affected by the length scale compared to the

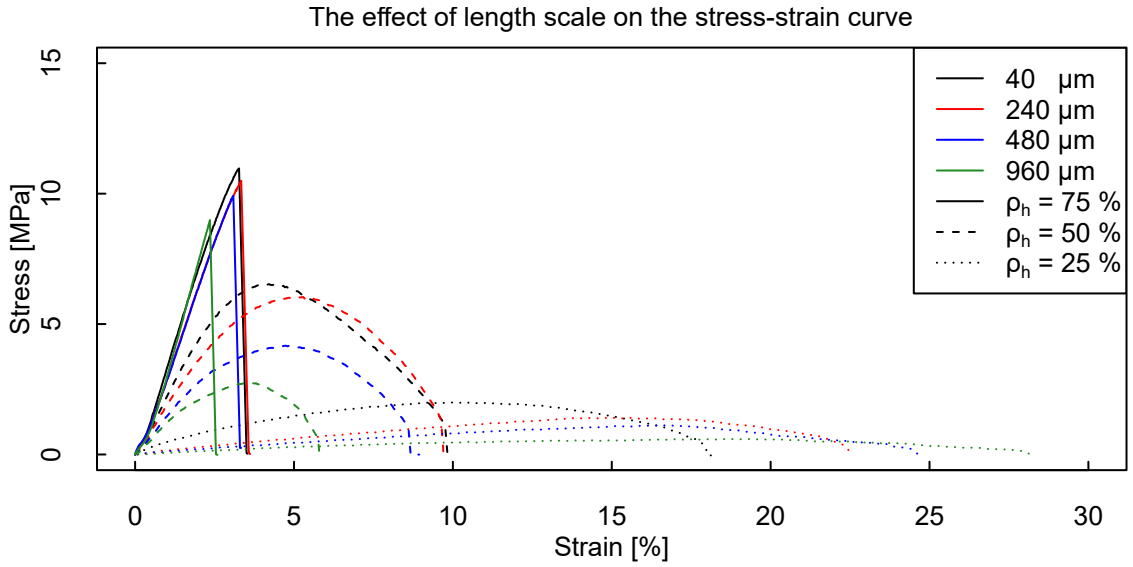


Figure 3.3: The effect of length scale on the stress-strain curves of the semi-ordered samples for three different hard material ratios. The graph only shows the samples that were tested as third.

other hard material ratios. The $\rho_h = 75\%$ samples with a voxel length of 40, 240 and 480 μm showed comparable stress-strain curves. The $\rho_h = 75\%$ samples with a voxel length of 960 μm fractured at a lower fracture stress and strain compared to the other length scales. However, the $\rho_h = 50\%$ samples were more affected by the length scale. For these samples, a smaller voxel length resulted in a higher fracture stress and strain. The fracture stress was 2.5 times higher for the $\rho_h = 50\%$ samples with a voxel length of 40 and 240 μm compared to the $\rho_h = 50\%$ samples with a voxel length of 960 μm. Lastly, the length scale influenced the stress-strain curves of the $\rho_h = 25\%$ samples as well. The $\rho_h = 25\%$ samples with a voxel length of 40 μm showed the highest fracture stress, whereas the $\rho_h = 25\%$ samples with a voxel length of 960 μm showed the highest final strain. In summary, the length scale affected the stress-strain curves in different ways, depending on the hard material ratio. A smaller length scale resulted in a higher stress, but not necessarily in a higher strain, this was dependent on the hard material ratio.

3.4. Hard-soft material arrangement

Figure 3.4 shows the effect of hard-soft material arrangement on the stress-strain curve for three different hard material ratios (75, 50 and 25 %) and for two different length scales (40 and 960 μm). The effect of hard-soft material arrangement on the stress-strain curve was dependent on the hard material ratio and the length scale. The hard-soft material arrangement affected the stress-curves of the $\rho_h = 75\%$ samples the least (Figure 3.4a and b). Additionally, the $\rho_h = 50\%$ samples with a voxel length of 40 μm obtained nearly similar stress-strain curves. However, the stress-strain curves of the $\rho_h = 50\%$ samples with a voxel-length of 960 μm was affected by the hard-soft material arrangement. The random arranged $\rho_h = 50\%$ samples with a voxel length of 960 μm achieved a lower fracture stress and higher final strain compared to the semi-ordered and ordered arranged samples. Lastly, the hard-soft material arrangement affected the stress-strain curves of the $\rho_h = 25\%$ samples. The final strain of the $\rho_h = 25\%$ samples was influenced by the hard-soft material arrangement. An ordered arrangement resulted in the highest final strain for the $\rho_h = 25\%$ samples with a voxel length of 40 μm (Figure 3.4a). However, an ordered arrangement resulted in the lowest final strain for the $\rho_h = 25\%$ samples with a voxel length of 960 μm (Figure 3.4b). In summary, the effect of hard-soft material arrangement was dependent on the hard material ratio and length scale. The hard-soft material arrangement mostly affected the $\rho_h = 50\%$ samples with a voxel length of 960 μm and $\rho_h = 25\%$ samples with a voxel length of 40 μm and 960 μm.

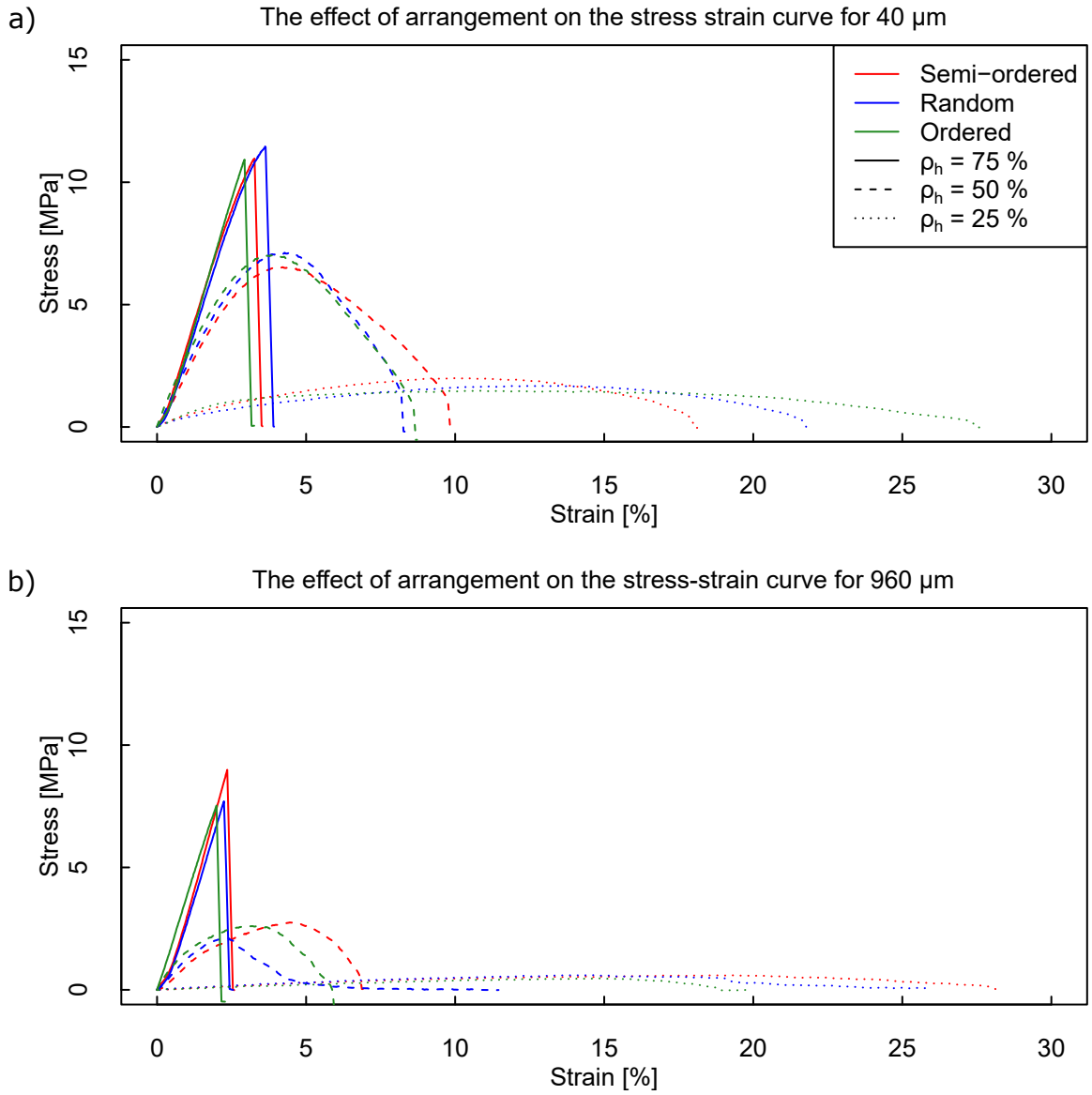


Figure 3.4: Effect of semi-ordered, random and ordered arrangements on the stress-strain curves for samples with a voxel length of 40 μm (a) and a voxel length of 960 μm (b). The graph only shows the samples that were tested as third.

3.5. Modulated effect

Figure 3.2, 3.3 and 3.4 show that the biomimetic design parameters had a modulated on the stress-strain curves. This section describes the modulated effect of the biomimetic design parameters on the fracture properties, which could be derived from the stress-strain curves. The modulated effects on the fracture properties, including stiffness, fracture stress, final strain and fracture toughness, is captured in different figures. First of all, the bar plots in Figure 3.5 and 3.6 show the effect of length scale on the fracture properties for the different hard-soft material arrangements and hard material ratios. Furthermore, table 3.2 shows how a decrease in length scale affected the fracture properties. The table shows the ratio of the mean value of the samples with a voxel length of 40 μm to a voxel length of 960 μm for all fracture properties. Subsequently, Figure 3.7 shows the stiffness (a) and fracture stress (b) against the fracture toughness for three hard material ratios on a logarithmic scale. Figure 3.8 shows the stiffness (a) and fracture stress (b) against the fracture toughness for the semi-ordered samples on a logarithmic scale. The effect of biomimetic design parameters on the stiffness, fracture stress, final strain and fracture toughness is discussed in more detail below with the help of the figures.

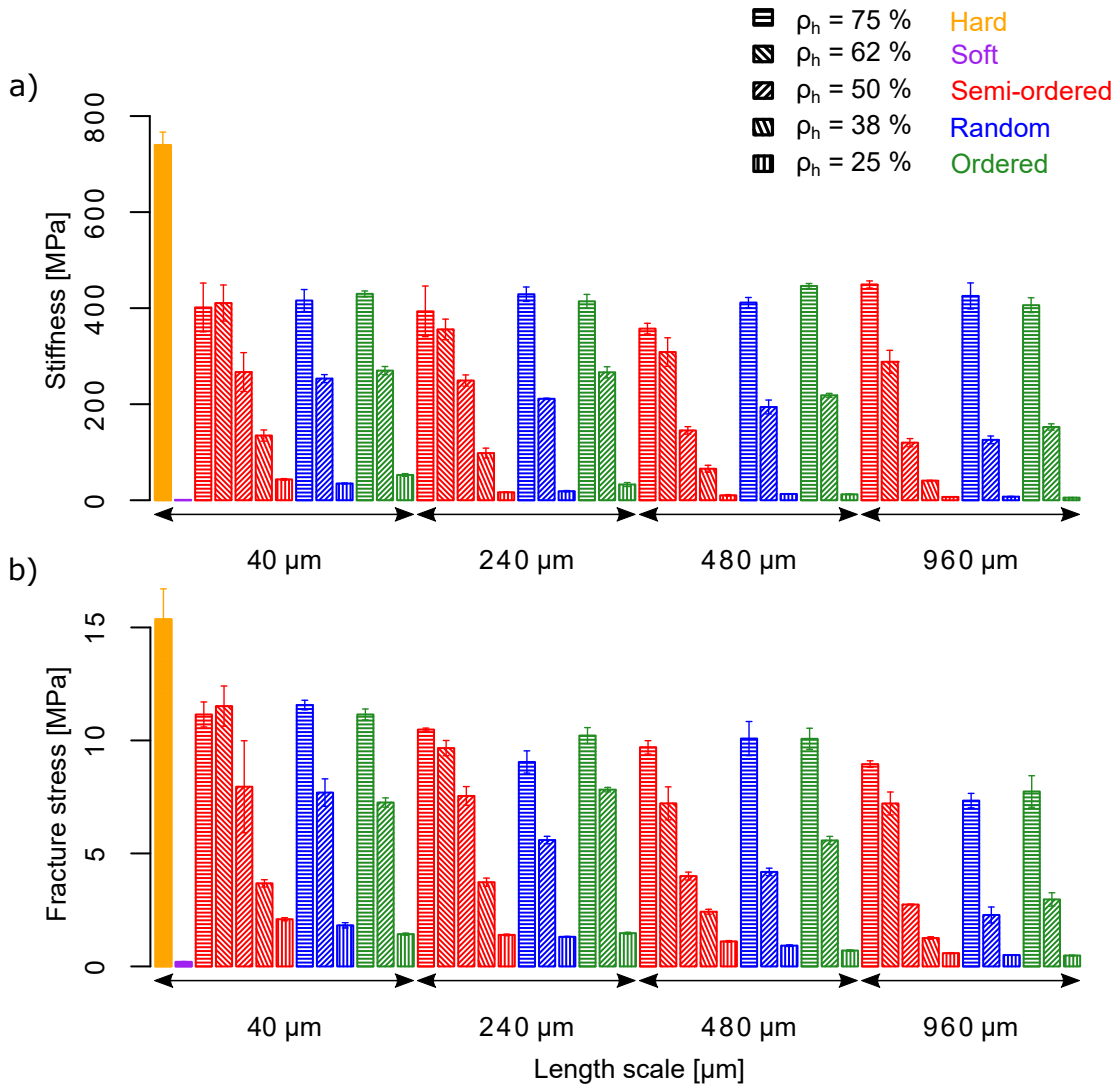


Figure 3.5: Bar plots of the stiffness (a) and the fracture stress (b) for different length scales. The bar plots show the effect of length scale on the fracture properties for all arrangements and hard material ratios. The mean value and standard deviation are shown.

3.5.1. Stiffness

The stiffness was mostly affected by the hard material ratio. Figure 3.5a shows that the hard material samples obtained the highest stiffness and the soft material samples the lowest. A decrease in hard material ratio resulted in a decrease in stiffness for nearly all material arrangements and length scales. The only exceptions were the $\rho_h = 62\%$ semi-ordered samples with a voxel length of 40 μm, that obtained a higher stiffness compared to the $\rho_h = 75\%$ samples with a similar arrangement and voxel length. Furthermore, the stiffness was also affected by the length scale. The effect of length scale on the stiffness was dependent on the hard material ratio and the hard-soft material arrangement. Figure 3.5a and 3.7a show that the length scale slightly affected the stiffness of the $\rho_h = 75\%$ samples. The stiffness of the semi-ordered and random organised $\rho_h = 75\%$ samples did not increase by a decrease in length scale (Table 3.2). The stiffness of the ordered $\rho_h = 75\%$ samples increased 1.1 times by decreasing the length scale. The length scale affected the stiffness of the $\rho_h = 38\%$ and $\rho_h = 25\%$ samples the most. The stiffness of the ordered $\rho_h = 25\%$ samples was increased 9.7 times by decreasing the voxel length from 960 μm to 40 μm (Table 3.2). The length scale influenced the semi-ordered samples the least. The increase in stiffness of semi-ordered samples was ranging between 1.4 and 3.3 times, depending on the hard material ratio (Table 3.2). The stiffness of the random organized $\rho_h = 25\%$ samples increased 4.7 times by printing at the smallest length scale

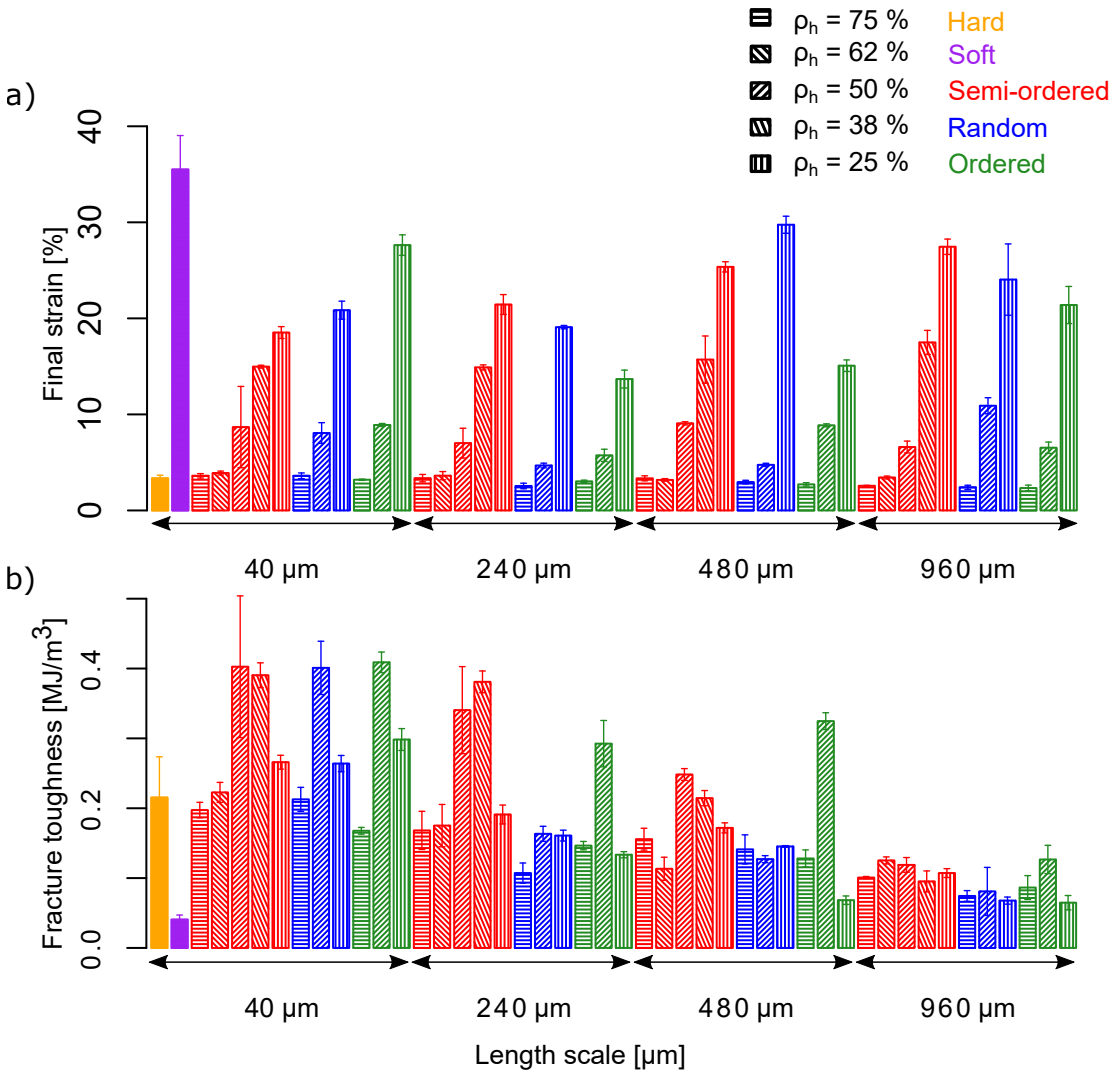


Figure 3.6: Bar plots of the final strain (a) and the fracture toughness (b) for different length scales. The bar plots show the effect of length scale on the fracture properties for all arrangements and hard material ratios. The mean value and standard deviation are shown.

(Table 3.2). In summary, the biomimetic design parameters had a modulated effect on the stiffness. Generally, a higher hard material ratio and a lower length scale resulted in a higher stiffness.

Rule of mixtures

It is not possible to achieve a higher stiffness than the highest value of the individual constituents, according to the rule of mixtures. The stiffness of a composite has to be within the upper and lower bound of the rule of mixtures. Equation (3.1) and (3.2) show respectively the upper and lower bound of the rule of mixtures.

$$\frac{E}{E_h} = (1 - \rho_h) * \frac{E_s}{E_h} + \rho_h \tag{3.1}$$

$$\frac{E}{E_h} = \frac{E_s}{\rho_h * E_s + E_h * (1 - \rho_h)} \tag{3.2}$$

In which E_h equals the hard material stiffness and E_s equals the soft material stiffness. Figure 3.9 shows that all stiffness values were within the upper and lower bound of the rule of mixtures.

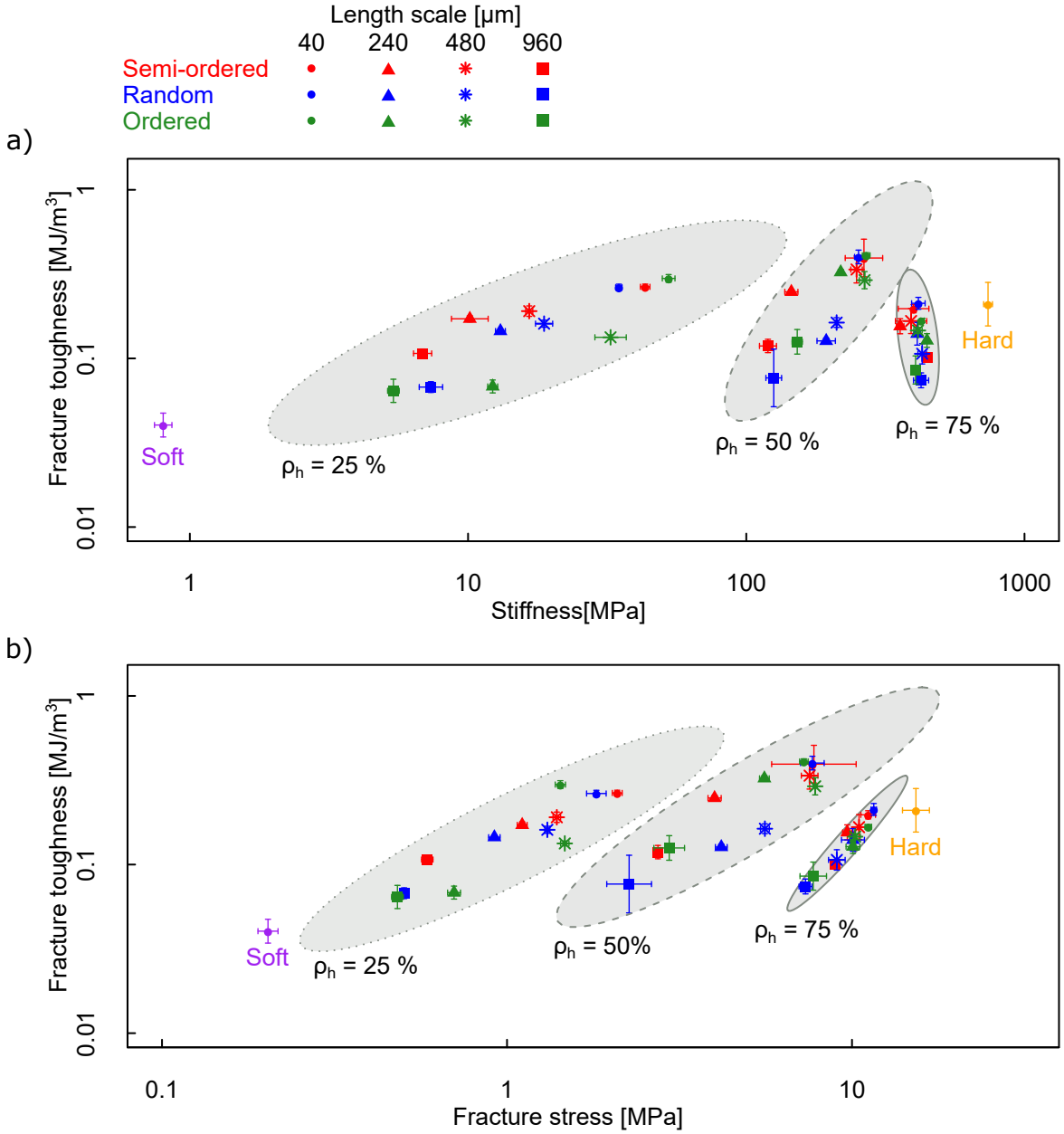


Figure 3.7: Fracture toughness against stiffness (a) and fracture stress (b) on a logarithmic scale. Ellipses with a 95 % confidence interval are drawn for three different hard material ratios. The mean value and standard deviation are shown.

3.5.2. Fracture stress

The hard material ratio affected the fractures stress the most. Figure 3.5b shows that the hard material samples obtained the highest fracture stress and the soft ones the lowest. An increase in hard material ratio resulted in an increase in fracture stress for nearly all material arrangements and length scales. The only exceptions were the $\rho_h = 62\%$ semi-ordered samples with a voxel length of 40 μm, which showed a higher fracture stress compared to the $\rho_h = 75\%$ samples with a similar arrangement and voxel length. Additionally, the length scale also affected the fracture stress. This effect was influenced by the hard material ratio and the hard-soft material arrangement. The length scale had the biggest effect on the fracture stress of the samples with the lowest hard-material ratio (Table 3.2). The fracture stress of the random arranged $\rho_h = 25\%$ samples increased 3.6 times by decreasing the length scale. The effect of length scale was less influenced by the hard-soft material arrangement compared to the hard material ratio. To summarize, the fracture stress was affected by the hard material ratio, length

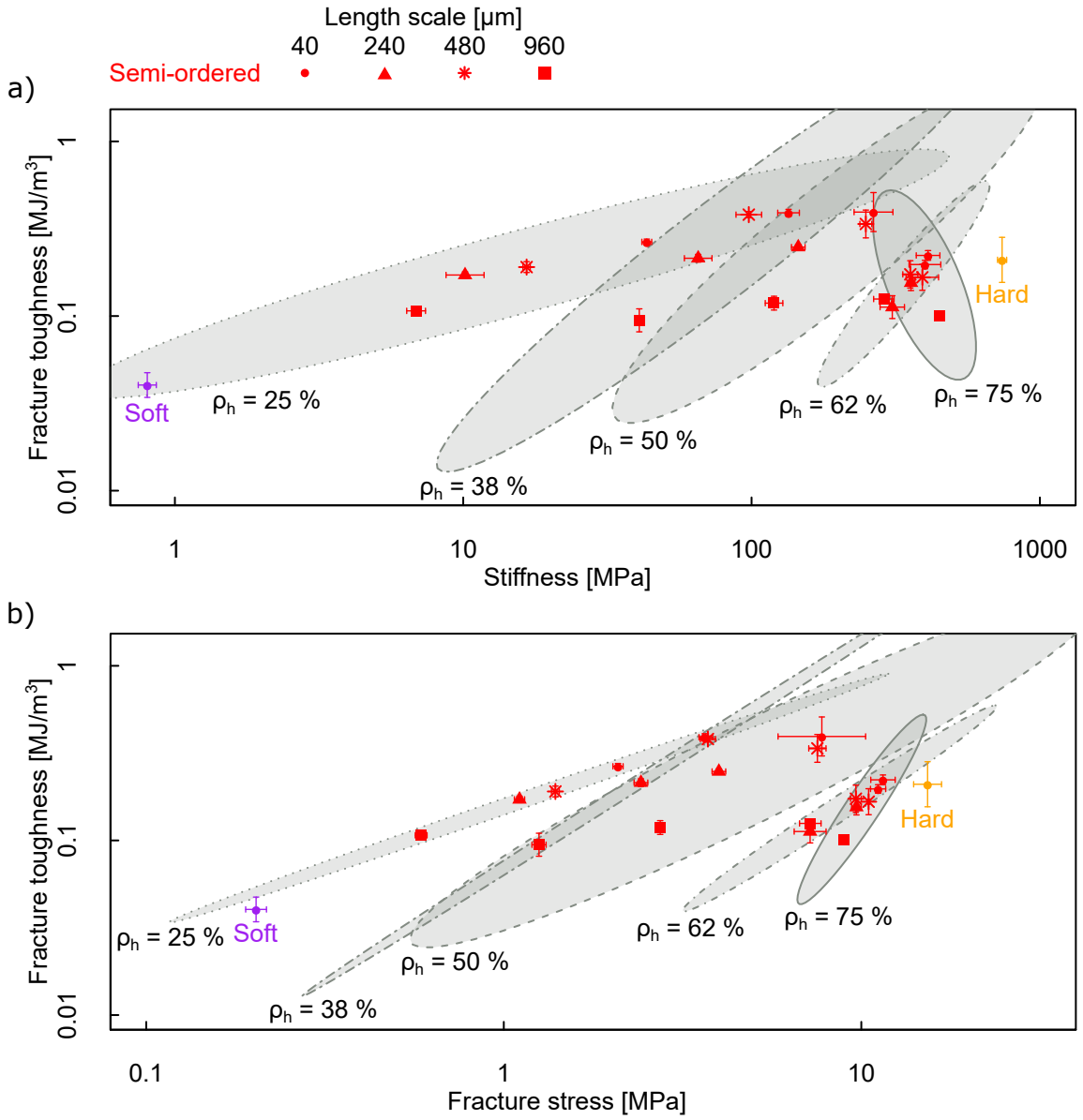


Figure 3.8: The fracture toughness against the stiffness (a) and the fracture stress (b) for the semi-ordered samples on a logarithmic scale. Ellipses with a 95 % confidence interval are drawn for five different hard material ratios. The mean value and standard deviation are shown.

scale and hard-soft material arrangement in a modulated way. In general, a higher hard material ratio and a lower length scale resulted in a higher fracture stress.

3.5.3. Final strain

Figure 3.6a shows that the final strain was affected by all three biomimetic design parameters. The soft samples obtained the highest final strain. Generally, a higher amount of soft material resulted in a higher final strain. However, the semi-ordered $\rho_h = 75\%$ samples with a voxel length of 480 μm obtained a higher final strain than the semi-ordered $\rho_h = 62\%$ samples with the same voxel length. Furthermore, it is remarkable that the hard material samples did not obtain the lowest final strain. Several $\rho_h = 75\%$ samples obtained a lower final strain than the hard samples (Appendix A). Additionally, Table 3.2 shows that the effect of length scale on the final strain was dependent on the arrangement and the hard material ratio. The final strain of all ordered arranged samples increased by decreasing the voxel length from 960 to 40 μm. The final strain of the semi-ordered $\rho_h = 38\%$ and $\rho_h = 25\%$

Table 3.2: The ratio of the mean value of the samples with a voxel length of 40 μm to the mean value of the samples with a voxel length of 960 μm. The table shows how a decrease in voxel length from 960 to 40 μm affected the properties, including stiffness, fracture stress, final strain and fracture toughness.

	Semi-ordered					Random			Ordered		
ρ_h [%]	75	62	50	38	25	75	50	25	75	50	25
Stiffness	0.89	1.4	2.2	3.3	2.6	0.96	2.0	4.7	1.1	1.8	9.7
Fracture stress	2.3	1.6	2.9	2.9	3.5	1.6	3.4	3.6	1.4	2.4	2.9
Final strain	1.4	1.1	1.3	0.86	0.67	1.5	0.74	0.87	1.4	1.4	1.3
Fracture toughness	2.0	1.7	3.3	3.9	2.3	3.0	5.0	3.7	1.9	3.2	5.0

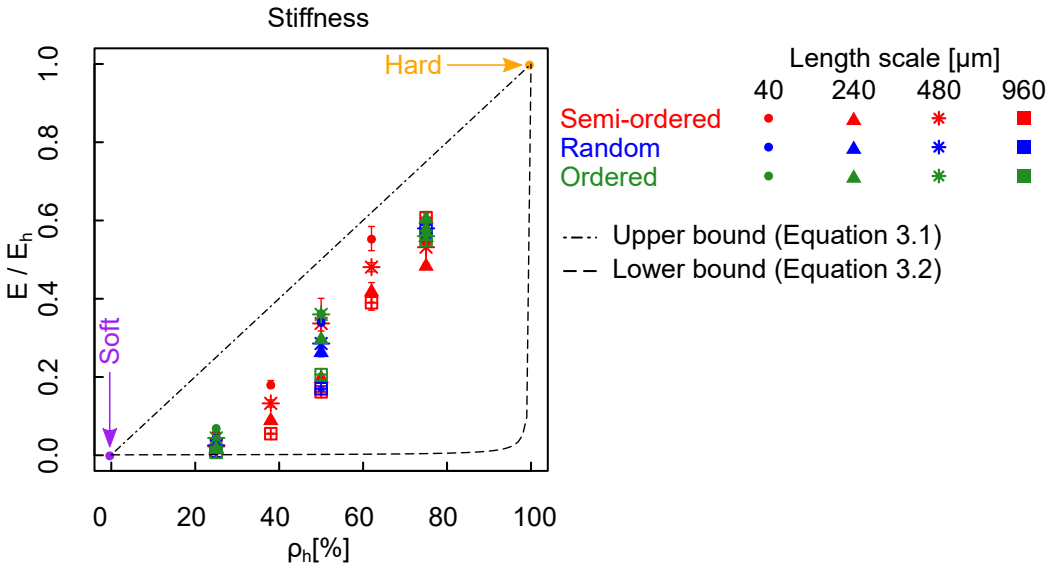


Figure 3.9: Comparison of the stiffness for different hard material ratios with the upper and lower bound of the rule of mixtures.

samples and the random arranged $\rho_h = 50\%$ and $\rho_h = 25\%$ samples decreased by decreasing the voxel length. In summary, the biomimetic design parameters had a modulated effect on the final strain. Specifically, a smaller amount of hard material resulted in a higher final strain.

3.5.4. Fracture toughness

Figure 3.6b shows that the fracture toughness was affected by all three biomimetic design parameters. The samples that contained an equal amount of hard and soft material ($\rho_h = 50\%$) obtained the highest fracture toughness for most hard-soft material arrangements and length scales. Furthermore, Table 3.2 shows that the samples with a smaller voxel length obtained a higher fracture toughness for all hard material ratios and hard-soft material arrangements. The effect of length scale on the fracture toughness was affected by both the hard-material ratio and the hard-soft material arrangement. The length scale had the most influence on the random organised $\rho_h = 50\%$ samples and ordered $\rho_h = 25\%$ samples.

Figure 3.6b shows that the fracture toughness of the hard samples was exceeded by thirteen hard-soft material samples. The following semi-ordered samples exceeded the fracture toughness of the hard samples: the $\rho_h = 62\%$, $\rho_h = 50\%$, $\rho_h = 38\%$, and $\rho_h = 25\%$ samples with a voxel length of 40 μm, the $\rho_h = 50\%$ and $\rho_h = 38\%$ samples with a voxel-length of 240 μm, and the $\rho_h = 50\%$ samples with a voxel-length of 480 μm. In addition, two random arranged samples exceeded the fracture toughness of the hard samples: the $\rho_h = 50\%$ and $\rho_h = 25\%$ samples with a voxel length of 40 μm. Lastly, four ordered arranged samples exceeded the fracture toughness of the hard samples: the $\rho_h = 50\%$ and $\rho_h = 25\%$ samples with a voxel length of 40 μm and the $\rho_h = 50\%$ samples with a voxel-length of 240 and 480 μm. The highest fracture toughness values were obtained by the $\rho_h = 50\%$ samples with a voxel length of 40 μm, independently of the hard-soft material arrangement.

In summary, the biomimetic design parameters had a modulated effect on the fracture toughness.

The fracture toughness of the hard-soft material samples could be improved compared to the fracture toughness of the individual constituents. Especially, the $\rho_h = 50\%$ samples with a voxel length of 40 μm obtained a high fracture toughness.

3.6. Digital image correlation

The DIC measurements of semi-ordered, random and ordered arranged samples were performed for three different hard material ratios (75, 50 and 25 %) and two different length scales (40 and 960 μm). Figure 3.10 shows the effect of hard-soft material arrangement on the ϵ_{yy} distribution for the different hard material ratios and length scales. The ϵ_{yy} was defined as the strain in the longitudinal direction. The frames were taken at the moment of highest applied load. This moment was equal to the last frame before fracture for the $\rho_h = 75\%$ samples.

Figure 3.10 shows that the strain distribution of the samples with a voxel length of 40 μm was independent of the hard-soft material arrangement. Plasticity occurred in front of the crack tip for the samples printed at native resolution. Additionally, the semi-ordered and ordered arranged $\rho_h = 50\%$ samples obtained comparable stress distributions for both voxel lengths. The hard-soft material arrangement affected the strain distribution of the samples with a voxel length of 960 μm. The strain distribution was not limited to the crack tip for these samples. Particularly, the random organised samples showed highly strained areas away from the crack tip.

Figure B.1 in appendix B shows the strain distribution in the X-direction. The minimum and maximum ϵ_{xx} values were relatively small compared to the ϵ_{yy} values.

3.6.1. Semi-ordered

The effect of length scale and hard material ratio on the strain distribution in the Y-direction was further analysed for the samples with a semi-ordered material arrangement. The strain distributions are shown for five different frames, as indicated in Figure 3.11. Figure 3.12 and 3.13 show the ϵ_{yy} distribution of the $\rho_h = 75\%$, $\rho_h = 50\%$ and $\rho_h = 25\%$ samples with a voxel length of 40 and 960 μm. The initial frame, the last frame before fracture, and three intermediate frames are shown for the $\rho_h = 75\%$ samples (Figure 3.12). The moment of highest applied force was different than the last frame before fracture for the $\rho_h = 50\%$ and $\rho_h = 25\%$ samples. The initial frame, the frame between the initial frame and the highest applied force, the frame at the highest applied force, a frame between the highest applied force and the moment before fracture and the last frame before fracture are shown for these samples (Figure 3.13). The $\rho_h = 25\%$ sample with a voxel-length of 960 μm elongated to much to show the complete stress concentration for all frames.

Figure 3.12 and 3.13 show that the initial frames were comparable for the different hard material ratios (75, 50 and 25 %). The minimum and maximum strain values were low at the initial frames of all samples, which was desirable. Nevertheless, the other frames show that the strain distribution of the semi-ordered samples was affected by hard material ratio and voxel length. The hard material ratio affected the plasticity region in front of the crack tip. A higher hard material ratio resulted in a smaller plasticity region in front of the crack tip. The $\rho_h = 75\%$ samples obtained the smallest plasticity region in front of the crack tip, whereas the $\rho_h = 25\%$ samples showed the largest plasticity region. Additionally, the $\rho_h = 25\%$ samples showed crack blunting, which was not feasible for the $\rho_h = 75\%$ samples. In addition to the hard material ratio, the length scale affected the strain distribution as well. The effect of length scale on the strain distribution was influenced by the hard material ratio. The length scale slightly influenced the strain distribution of the $\rho_h = 75\%$ samples. The strain was concentrated in front of the crack tip for the $\rho_h = 75\%$ sample with a voxel length of 40 μm, and was mostly concentrated in front of the crack tip for the $\rho_h = 75\%$ sample with a voxel length of 960 μm. In addition, the strain distribution was concentrated in front of the crack tip for $\rho_h = 50\%$ samples. However, Figure 3.13 shows that the length scale affected the fracture path of these samples. The fracture path of the $\rho_h = 50\%$ sample with a voxel length of 40 μm propagated through the middle, whereas the fracture path of the $\rho_h = 50\%$ sample with a voxel length of 960 μm branched a few times. The voxel length had the most influence on the strain distribution and the fracture path of $\rho_h = 25\%$ samples. The strain was not only concentrated in front of the crack tip for the $\rho_h = 25\%$ sample with a voxel-length of 960 μm. The strain was concentrated in different regions across the material for this sample, as shown by the second frame of the $\rho_h = 25\%$ sample with a voxel-length of 960 μm. The $\rho_h = 25\%$ sample with a voxel length of 40 μm showed a flat, straight fracture path, whereas the $\rho_h = 25\%$ sample with a voxel

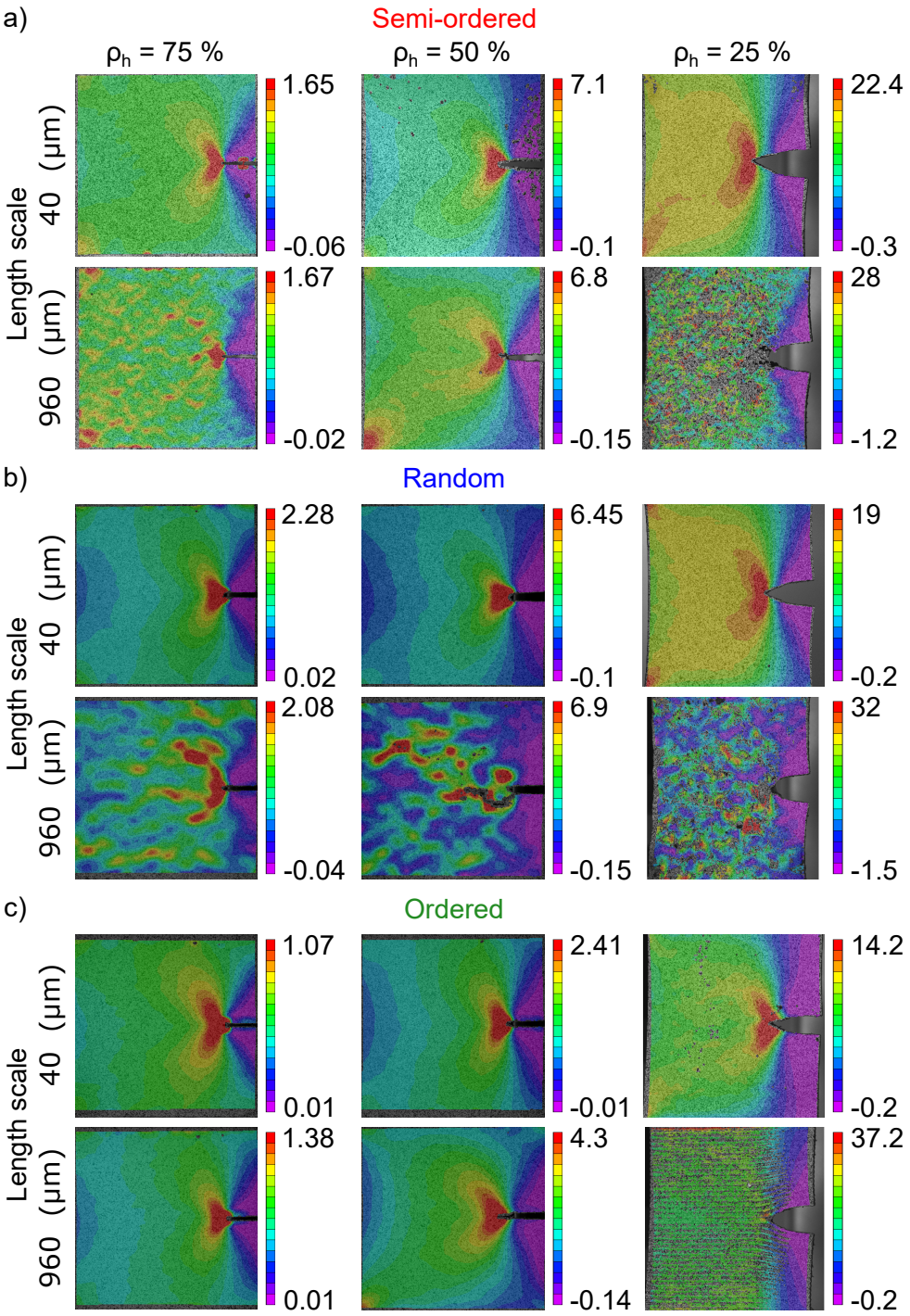


Figure 3.10: Strain distribution in the Y-direction at the moment of maximum applied force for a semi-ordered (a), random (b) and ordered (c) arrangement. The strain distributions are shown for three different hard material ratios and two different length scales. The minimum and maximum strain values are given in percentages at the right side of the frames.

length of 960 μm did not fracture in a straight line.

In summary, the strain distributions were affected by the biomimetic design parameters in a modulated way. The hard-soft material arrangement and hard material ratio affected the strain distributions especially at higher length scale Generally, the samples with a smaller voxel length and smaller hard material ratio obtained a larger plasticity zone in front of the crack tip.

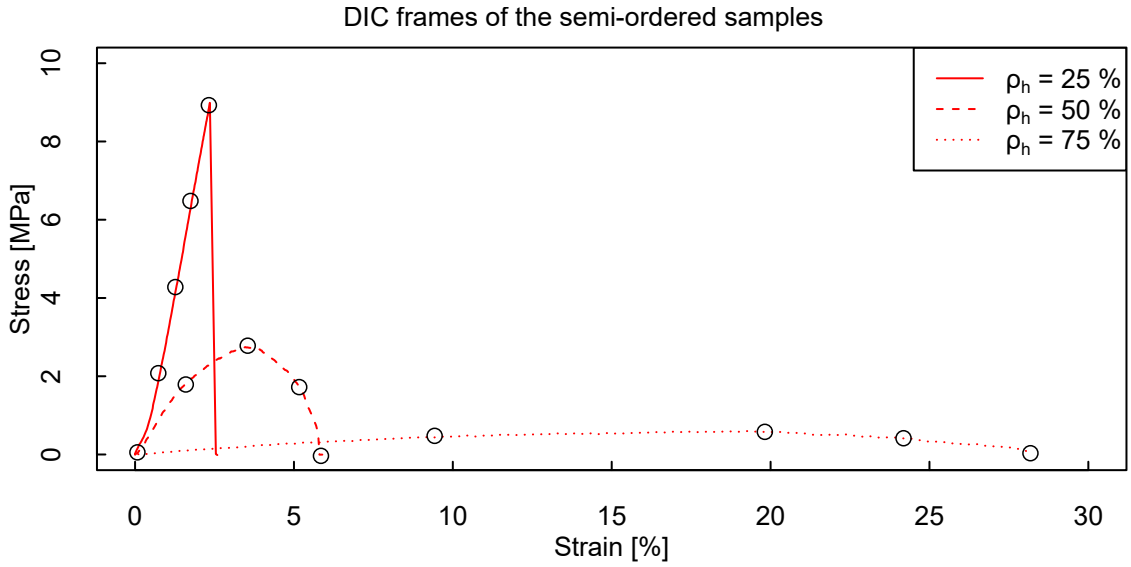


Figure 3.11: Stress-strain curves of the semi-ordered samples with a voxel length of 960 μm. The graph shows at which five moments the frames in Figure 3.12 and 3.13 are taken for the different hard material ratios.

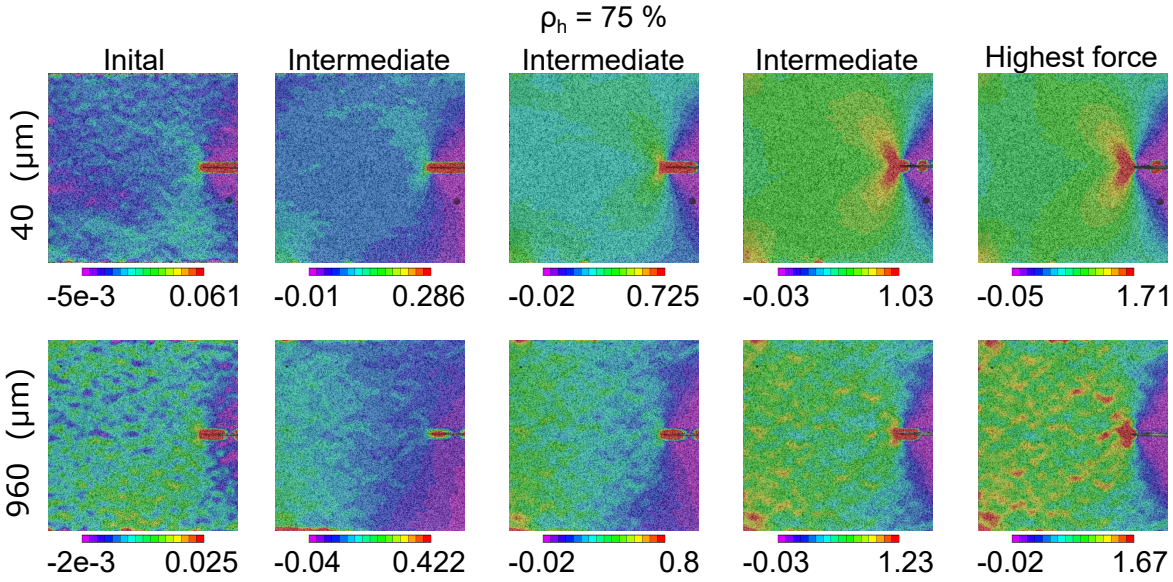


Figure 3.12: Strain distributions in the Y-direction of the semi-ordered $\rho_h = 75\%$ samples for different length scales. The strain distributions are given for five different frames, which are the initial frame, three intermediate frames and the frame of highest applied force. The minimum and maximum strain values are given in percentages below the frames.

3.7. Digital microscope

Digital microscopy images were taken to study the effect of biomimetic design parameters on the fracture path. Figure 3.14 shows the fracture paths of a hard and a soft sample. The hard sample showed crack branching, whereas the soft sample obtained an almost straight fracture path. The crack surfaces of the two samples differed as well. The area in front of the crack tip of the hard sample was damaged by a high stress concentration. The crack surface of the soft sample showed micro-cracks at the interface.

Figure 3.15, 3.16 and 3.17 show respectively the crack paths of the semi-ordered, random and ordered arranged samples at two magnifications (20x and 200x). These figures show that the effect of hard-soft material arrangement on the fracture path was influenced by the hard material ratio and the length scale. The samples with a voxel length of 40 μm showed a similar crack path for the different

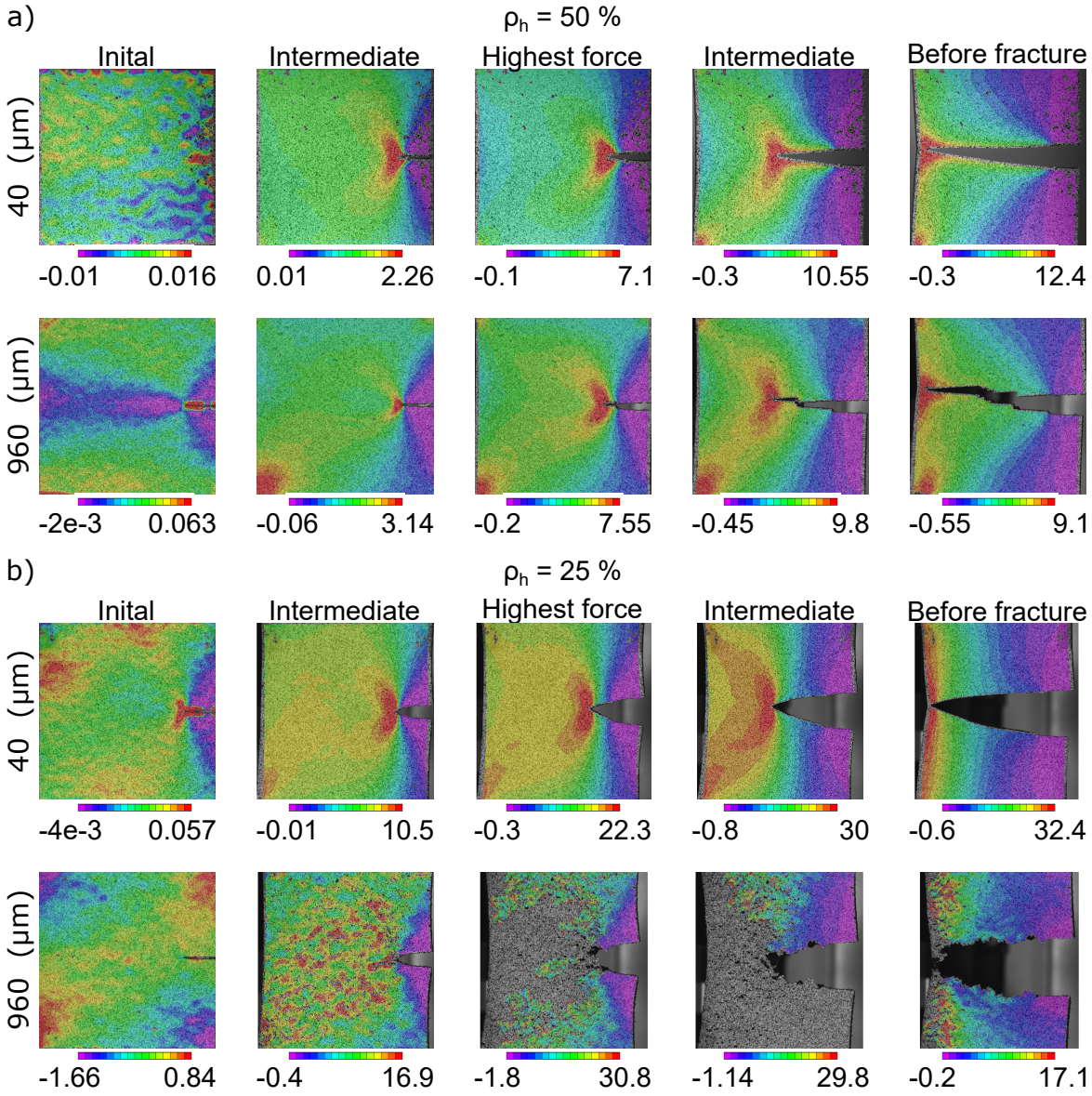


Figure 3.13: Strain distributions in the Y-direction of the semi-ordered $\rho_h = 50\%$ (a) and $\rho_h = 25\%$ (b) samples for different length scales. The strain distributions are given for five different frames, which are the initial frame, the frame of highest applied force, one frame before fracture and two intermediate frames. The minimum and maximum strain values are given in percentages.

hard-soft material arrangements. The $\rho_h = 75\%$ samples with a voxel length of 40 μm showed crack branching for all material arrangements. The crack path was an almost sharp line for the $\rho_h = 50\%$ and $\rho_h = 25\%$ samples with a voxel length of 40 μm. In addition, the crack paths of the samples with a voxel length of 960 μm were affected by the hard-soft material arrangement. The $\rho_h = 75\%$ samples with a 960 μm voxel length showed crack branching for the semi-ordered and the ordered arrangement. The randomly organized $\rho_h = 75\%$ samples with a voxel length of 960 μm did not show crack branching. The crack paths of the semi-ordered and ordered samples with a voxel length of 960 μm were similar for a hard material ratio of 50 %. These samples fractured almost straight through the hard-soft material interfaces. Crack propagation through one of the constituents was not possible, due to the hard-soft checkerboard arrangement of these samples. The fracture path of the random arranged $\rho_h = 50\%$ sample propagated through the soft material. Similarly, the fracture path of all $\rho_h = 25\%$ samples with a voxel length of 960 μm propagated through the soft material phases. This was a straight line for the ordered $\rho_h = 25\%$ sample with a voxel length of 960 μm, due to the hard-soft

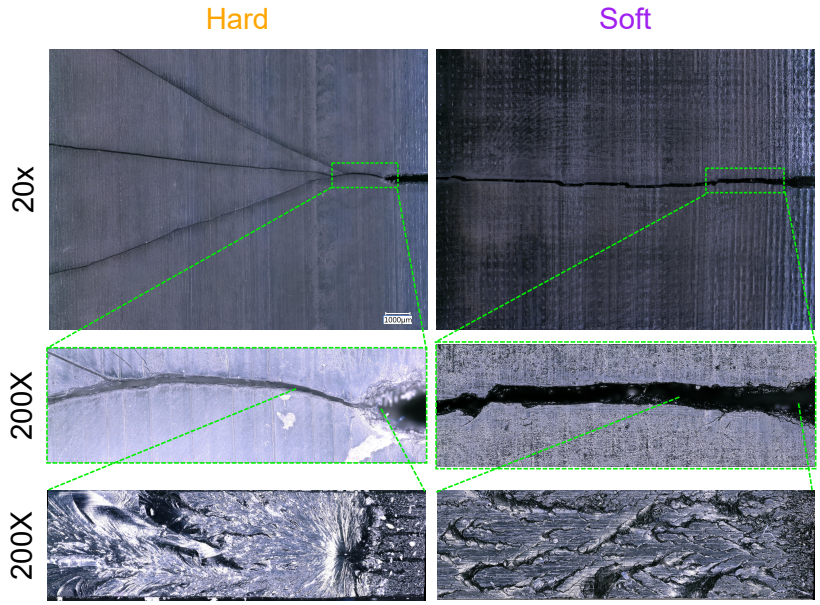


Figure 3.14: Microscopy images of the hard (left) and soft (right) samples. Images of the crack path were taken with a 20x and 200x magnification. The image of the crack surface was taken with 200x magnification.

material arrangement.

Figure 3.15 also shows the crack surfaces of the semi-ordered samples. The hard material ratio affected the crack surface the most. The crack surfaces of the $\rho_h = 75\%$ samples were damaged in front of the crack tip by a high stress concentration, which is comparable to the crack surface of the hard sample. The $\rho_h = 50\%$ and the $\rho_h = 25\%$ samples with a voxel length of 40 μm showed micro-cracks at the crack surface. This fracture behaviour is comparable to the micro-cracks at the crack surface of the soft sample.

Figure 3.18 shows the effect of length scale on the fracture path of semi-ordered samples with a hard material ratio of 25 %. The hard and soft material phases of the samples with a voxel length of 40 μm were not distinguishable. The hard and soft material phases were distinguishable starting at a length scale of 240 μm. These images show that the crack path tended to propagate through the soft material. This was easier for the samples with a higher voxel length. A lower length scale resulted in a straighter fracture path (Figure 3.18).

In summary, the hard-soft material arrangement, hard material ratio and length scale affected the fracture path in different ways. The crack tended to propagate through the soft material, which was more easier for the samples with a higher voxel length and a higher amount of hard material.

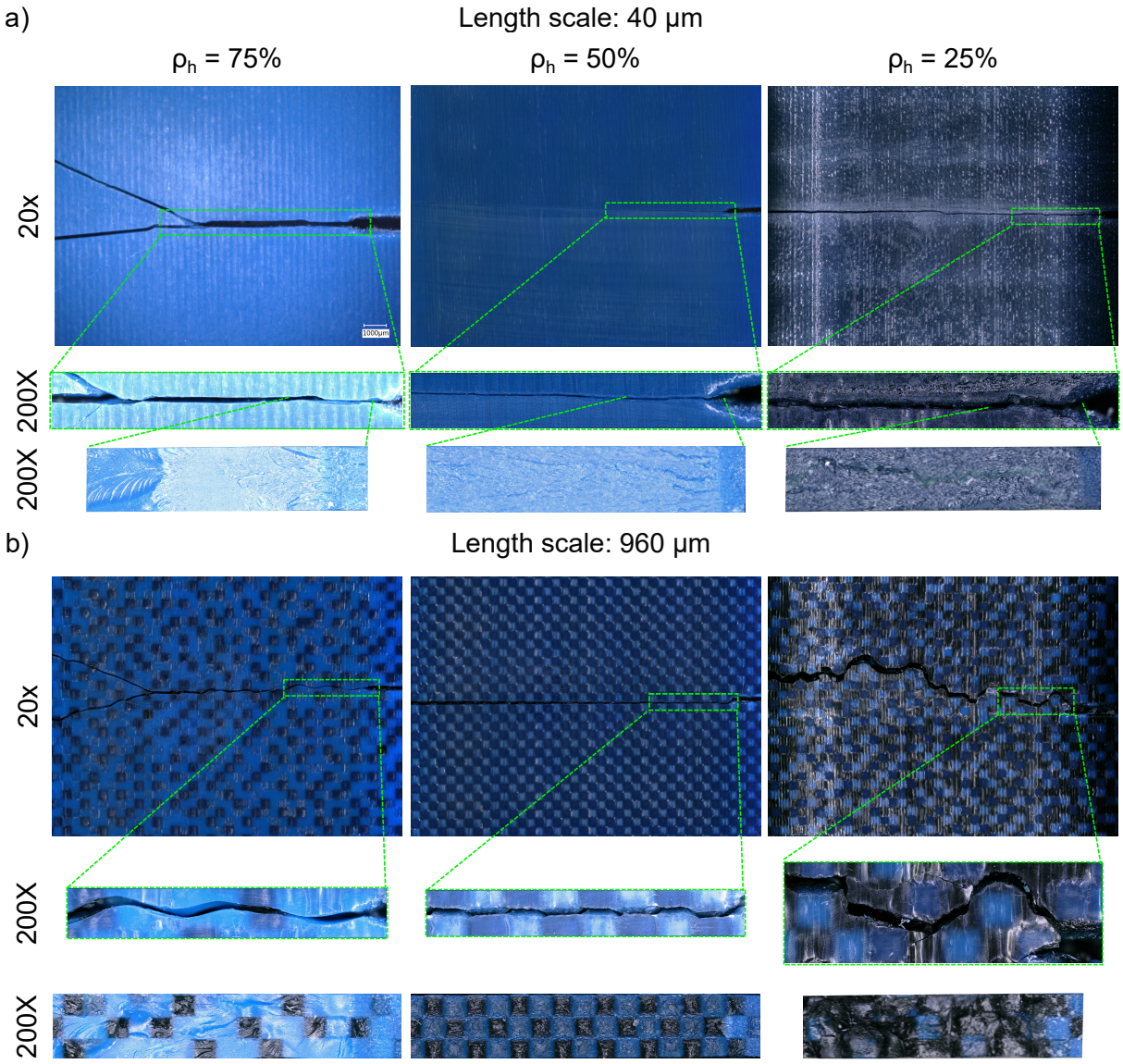


Figure 3.15: Microscopy images of the semi-ordered arranged samples with a voxel length of 40 and 960 μm for three different hard material ratios. Images of the crack path were taken with a 20x and 200x magnification. The third row shows the crack surface with a 200x magnification.

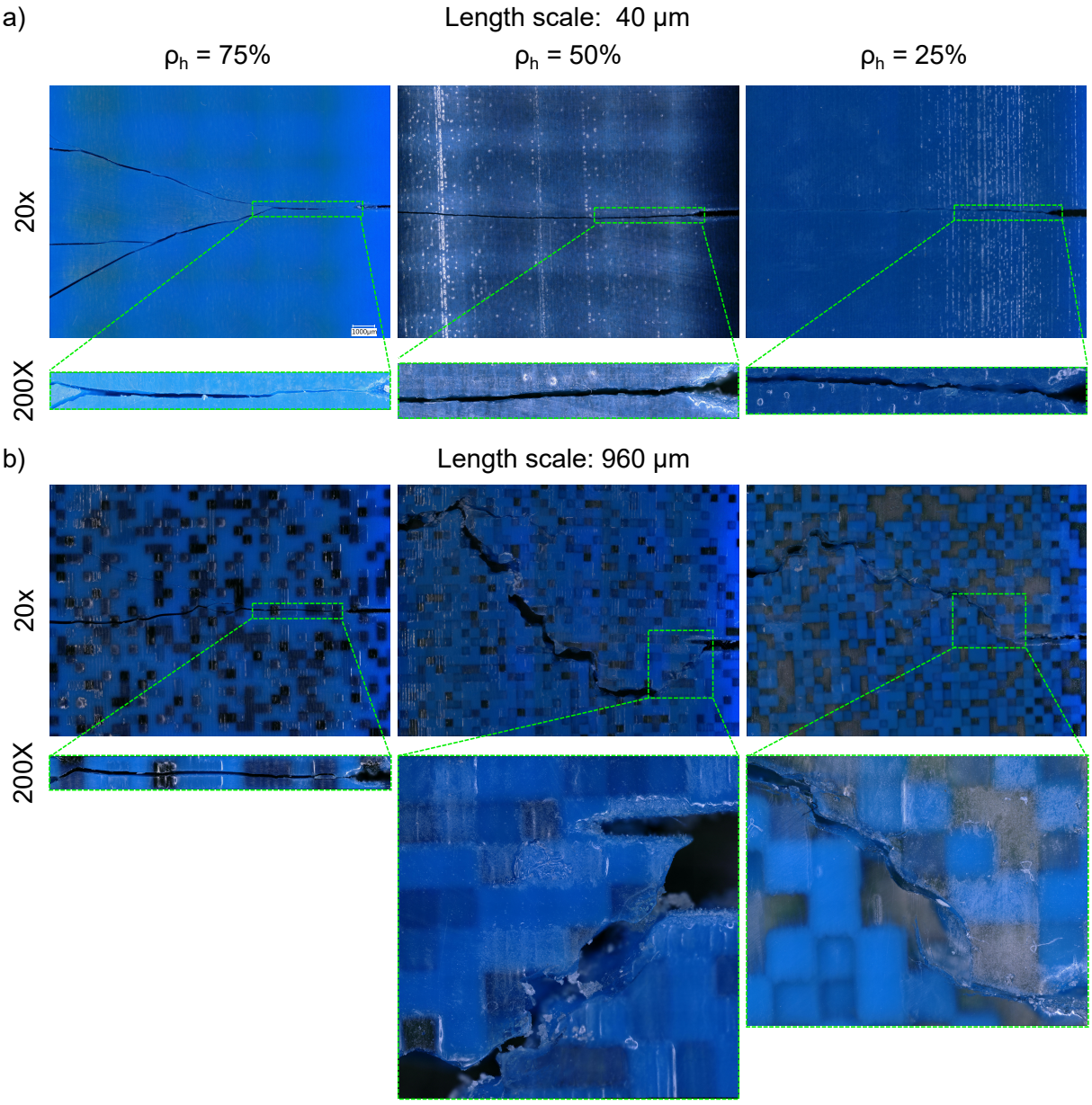


Figure 3.16: Microscopy images of the random arranged samples with a voxel length of 40 and 960 μm for three different hard material ratios. Images of the crack path were taken with a 20x and 200x magnification.

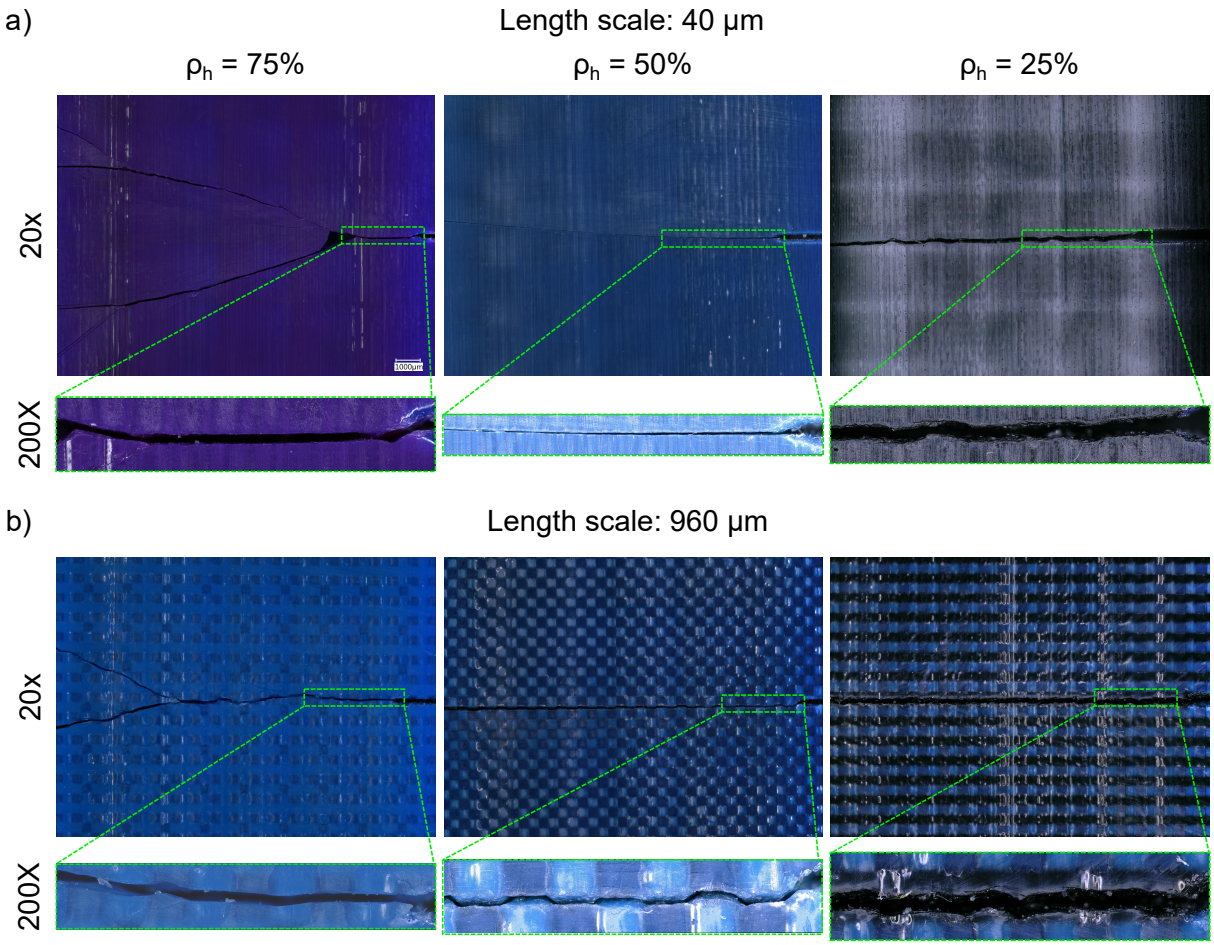


Figure 3.17: Microscopy images of the ordered arranged samples with a voxel length of 40 and 960 μm for three different hard material ratios. Images of the crack path were taken with a 20x and 200x magnification.

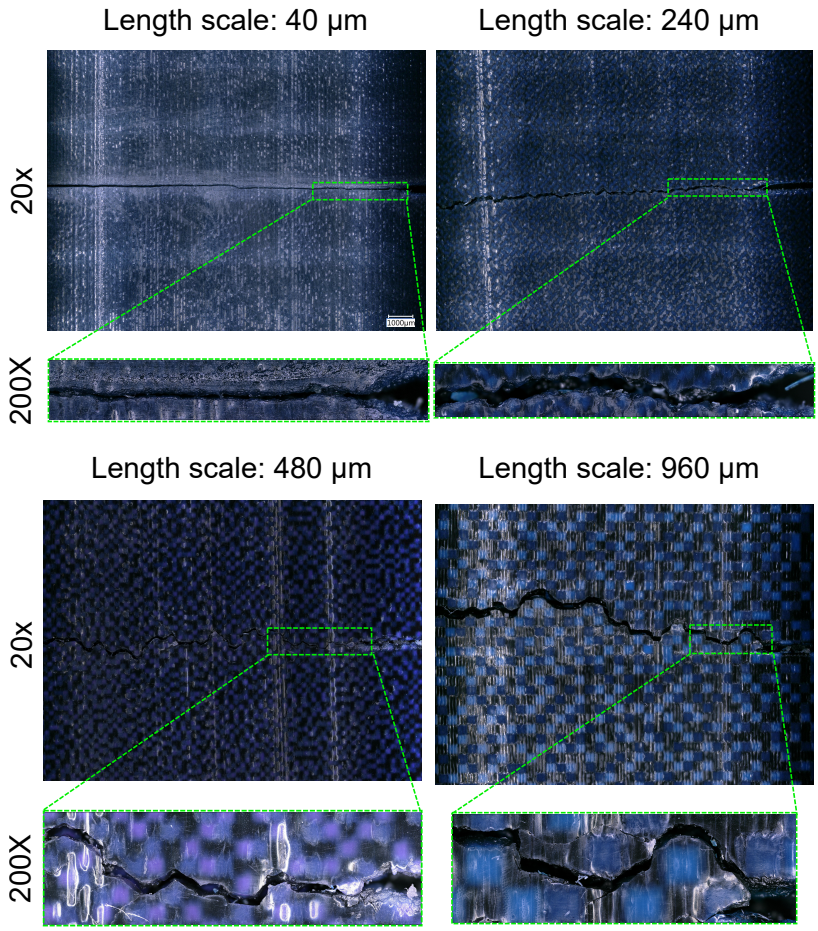


Figure 3.18: Microscopy images of the samples with a semi-ordered arrangement with a hard material ratio of 25 % for four different length scales. Images of the crack path are taken with 20x and 200x magnification.

4

Discussion

From the results can be concluded that the biomimetic design parameters affected the fracture properties in different ways. Figure 4.1 shows the modulated effect of hard material ratio and length scale on the stiffness, fracture stress and fracture toughness. The arrows show how a decrease in length scale affected the fracture properties. A decrease in length scale resulted in an increase in fracture toughness and fracture stress. Besides the effect of length scale, Figure 4.1 also shows the effect of hard material ratio. An increase in hard material ratio resulted in an increase in stiffness and fracture stress for almost all hard-soft material arrangements and length scales. The hard samples showed the highest stiffness and fracture stress. However, the fracture toughness of the hard samples could be improved by the addition of soft material phases.

This chapter discusses the isolated and modulated effects of the different biomimetic design parameters on the fracture properties. Subsequently, the results are compared with previous literature studies on natural materials. Additionally, the limitations of this study and recommendations are given. This chapter closes with future research directions.

4.1. Monolithic samples

The monolithic hard and soft material samples showed opposite fracture properties. The hard material sample showed the highest stiffness and fracture stress, whereas the soft material showed the lowest stiffness, fracture stress and fracture toughness. Additionally, the hard samples showed crack branching, whereas the soft samples showed crack blunting. Crack blunting is a mechanism that decreases the crack tip stress by increasing the effective radius of the crack tip [85]. The hard and soft samples weighed both 32 grams, which means that the material phase did not affect the sample weight.

The stiffness ratio between the two constituents is an important parameter of hard-soft materials. The soft material phases alleviate stress concentrations if the stiffness ratio of the constituents is at least five, according to previous literature studies [11, 11, 25, 32]. Furthermore, a high stiffness ratio would result in crack stopping in flawed materials [11, 32]. Here, the stiffness ratio between the monolithic samples was equal to 921.

4.2. Hard material ratio

The hard material ratio affected the fracture properties in different ways. A higher hard material ratio resulted in a higher stiffness and fracture stress, and in a lower final strain. However, the monolithic hard samples did not obtain the lowest final strain, which was not expected. This could be explained by the toe region at the beginning of the stress-strain curves of the hard samples, due to the accuracy of the test set-up. Generally, the materials with an equal amount of hard and soft material ($\rho_h = 50\%$) showed the highest fracture toughness. This means that a significant amount of hard and soft material phases was required to obtain a high fracture toughness. The hard material phases carried stresses, resulting in a higher fracture stress, whereas the soft material phases absorbed energy by deformation, resulting in a high final strain. A high fracture stress and finals strain are required for a high fracture toughness. The samples with a higher amount of soft material showed a larger plasticity zone in front

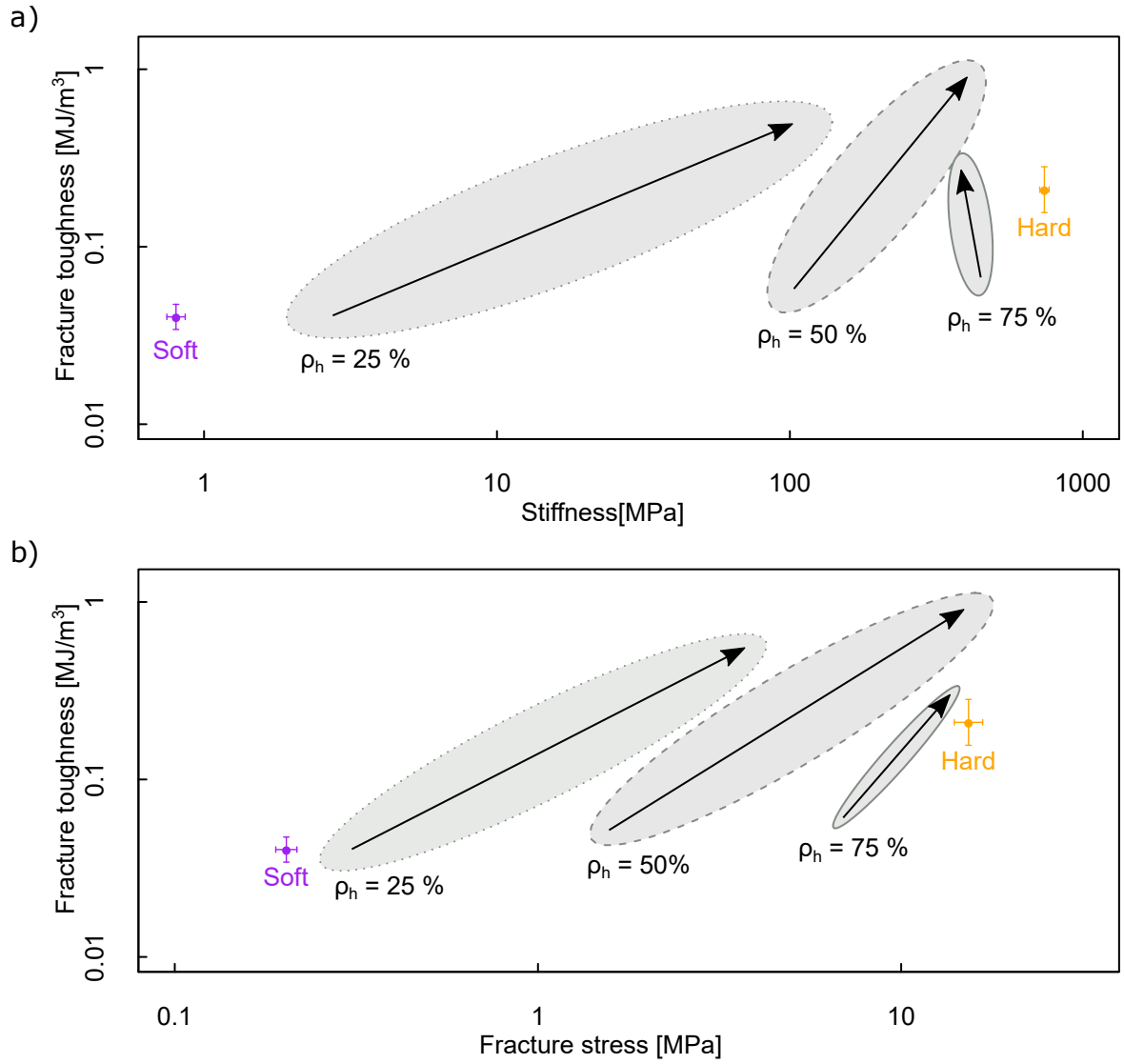


Figure 4.1: The effect of hard material ratio and length scale on the fracture properties on a logarithmic scale. The fracture stress (a) and the stiffness (b) against the fracture toughness are shown. Ellipses with a 95 % confidence are drawn for three different hard material ratios. The arrows show how a decrease in length scale, starting at the tail, affected the fracture properties.

of the crack tip. The plasticity zone in front of the crack tip is an important toughening mechanism [2]. In addition, the samples with a higher amount of soft material showed more crack blunting, which decreases the crack tip stress.

4.3. Length scale

The arrows in Figure 4.1 illustrate the influence of length scale on the fracture properties. A smaller length scale resulted in a higher fracture stress and fracture toughness. However, a smaller length scale did not necessarily result in a higher stiffness and final strain. Table 3.2 shows that a smaller length scale did not result in a higher stiffness for the semi-ordered and random arranged $\rho_h = 75\%$ samples. Additionally, a smaller length scale did not result in a higher final strain for the semi-ordered $\rho_h = 38\%$ and $\rho_h = 25\%$ samples, and also not for the random arranged $\rho_h = 50\%$ and $\rho_h = 25\%$ samples.

The effect of length scale on the fracture properties was affected by the hard material ratio. The length scale had a larger effect on the properties if a significant amount of soft material was present. As a result, the samples with a smaller hard material ratio resulted in a higher range of fracture properties.

Crack propagation through soft material phases was more difficult for the samples printed at a smaller length scale, resulting in higher fracture properties for the samples printed at native resolution. A soft material phase voxel was less influenced by its adjacent hard material phase voxels at a higher length scale. As a result, crack propagation through the soft material phase was easier at a higher length scale. In addition, a crack could propagate longer through a soft material phase before being blocked by a hard material phase voxel at higher length scale.

The fracture toughness of the ordered $\rho_h = 50\%$ samples is higher for the samples with a voxel length of 480 μm compared to samples with a voxel length of 240 μm, which was not expected. This could be explained by the accuracy of the test set-up, which is further discussed in Section 4.8 that describes the limitations of this research.

4.4. Hard-soft material arrangement

The results showed that length scale and hard material ratio had a greater influence on the fracture properties than hard-soft material arrangement. The hard-soft material arrangement mostly affected the final strain compared to the other fracture properties. Figure 3.7 shows that the hard-soft material arrangement which resulted in the highest fracture property was dependent on the other two design parameters. The crack paths of the different arrangements show that the crack path can be guided by the arrangement (Figure 3.15, 3.16 and 3.17). For example, the $\rho_h = 50\%$ samples with a ordered hard-soft material arrangement and voxel length of 960 μm resulted in a low fracture toughness. These samples fractured from the crack tip in a horizontal line through the middle and through the soft material phase. As a result, crack deflection did not occur in these samples.

The hard-soft material arrangement was distributed in all directions, which resulted in an heterogeneous arrangement of hard and soft material phases in all directions. This is advantageous compared to a transversely isotropic arrangement according to Fratzl et al. [32]. The influence of the heterogeneous hard-soft material distribution is visible on the microscopy images. The crack surfaces in Figure 3.15 show that micro-cracks were arrested across the interface. This toughening mechanism is also found in natural materials.

Voxel-based AM enables printing of digital materials. A digital material is composed of a mixture of different materials on the microscopic scale which results in a new material on the macroscopic scale [70]. This study shows that the fracture properties of a digital material are slightly dependent on the voxel arrangement at microscopic scale.

4.5. Digital image correlation

The strain concentrations of different samples were analysed with DIC measurements. Strain concentrations occurred in front of the crack tip for all samples at the beginning of test, which is due to the presence of the crack. The strain concentrations of the samples differed during testing. First of all, the size of the plasticity zone decreased by increasing the amount of hard material ratio and increasing the voxel size. The plasticity zone in front of the crack tip, which dissipates energy, is an important toughening mechanism [1, 2]. A higher plasticity zone resulted in more energy dissipation, which increases the fracture toughness. This explains why a higher length scale resulted in a lower fracture toughness. The 960 μm samples showed highly strained areas away from the crack tip. These highly strained areas occurred in the soft material phases. Especially, the random arranged $\rho_h = 75\%$ and $\rho_h = 50\%$ showed highly strained areas away from the crack tip compared to the semi-ordered and ordered $\rho_h = 75\%$ and $\rho_h = 50\%$ samples. This explains the lower fracture toughness of these random samples compared to the semi-ordered and ordered samples with the same hard material ratio. With respect to the strain distribution, the samples with a voxel length of 960 μm showed a higher difference in strain distribution compared to the samples with a voxel length of 40 μm, explaining the greater difference in fracture properties for the samples printed at higher length scale.

The DIC images in Appendix B show that the ϵ_{xx} was significantly small compared to the ϵ_{yy} at the moment of highest applied load. A low ϵ_{xx} indicates that the test set-up was sufficient.

DIC measurements have been performed in previous literature studies [37, 39, 42, 72]. These studies show that the highly strained areas occurred in the soft material phases, which is comparable to this study. Furthermore, the strain concentration was not only concentrated in front of the crack tip in previous studies, which is comparable to the highly strained areas away from the crack tip for the samples with a voxel length of 960 μm in this study.

The $\rho_h = 25\%$ semi-ordered sample with a voxel-length of 960 μm elongated too much to obtain the complete stress concentration. The subset and step size were not adjusted for this sample. These parameters were kept constant for the different DIC analyses.

4.6. Digital microscope

The effect of biomimetic design parameters on the fracture path was studied with a digital microscope. The biomimetic design parameters affected the fracture path in different ways. First of all, the hard material ratio affected the fracture path. The $\rho_h = 75\%$ samples and pure hard material samples showed crack branching during fracture, which increased the path length. The microscope images of the $\rho_h = 50\%$ and $\rho_h = 25\%$ samples showed that the fracture path tended to propagate through soft material phases, if at least 50 % of soft material was present. In addition, the length scale affected the fracture path. Particularly, the fracture path of the random arranged samples was affected by the length scale. Furthermore, the samples with a voxel length of 960 μm showed a greater difference in fracture paths compared to the samples with a voxel length of 40 μm . This explains the greater difference in fracture properties for the samples printed at higher length scale. Lastly, the hard-soft material arrangement affected the fracture path of the samples with a voxel length of 960 μm. The microscope images of these samples show that the hard-soft material arrangement can be used to guide crack propagation.

The samples did not tend to fracture at the hard-soft material interface, validating sufficient adhesion between the soft and hard material phases. This was also reported in previous literature studies [47, 72]. However, the semi-ordered and ordered $\rho_h = 50\%$ samples with a voxel length of 960 μm fractured at the hard-soft material interfaces. A fracture path through the soft material phases was not possible for these samples, due to the checkerboard hard-soft material arrangement of these samples.

Th fracture behaviour of the samples is comparable to previous literature studies that used the same printer and materials [11, 34, 35, 37, 39, 40, 42, 44, 47]. These studies showed that the crack tends to propagate through soft material phases. Furthermore, the samples of previous literature studies did not fracture at the hard-soft material phases either.

4.7. Comparison

The fracture properties obtained in this study are compared to previous literature studies. In addition, the fracture behaviour of the samples is compared with the behaviour of natural materials.

4.7.1. Previous literature studies

First of all, the fracture properties of the monolithic samples are compared to previous literature studies. The fracture stress of the monolithic hard and soft samples are comparable to the fracture stresses reported by Dimas et al. [11]. They have tested the monolithic materials in a similar way. The final strain of the soft material is also similar to the final strain that was obtained by Dimas et al. [11]. However, the final strain of the hard sample is higher in this study. This can be explained by the toe region at the beginning of the stress-strain curves of the hard samples (Figure 3.1), which is caused by the accuracy of the test set-up, as discussed in Section 4.8.

The fracture properties of the hard-soft material samples are in range with previously reported fracture properties, that were obtained with a similar test set-up. [11, 39, 40, 42, 47]. Figure 4.2 compares the fracture stress and fracture toughness obtained in this study with two previous literature studies [42, 47]. Libonati et al. have studied the fracture properties of bone-inspired materials with circular or elliptical soft osteons in a stiff matrix [47]. The hard material ratio of the stiff matrix was equal to 60 % in their study. They have obtained a comparable fracture toughness. However, Libonati et al. obtained a lower fracture stress compared to this study [47]. In addition, Gu et al. have studied the fracture properties of nacre-inspired materials. They have studied the effect of hard material ratio and mineral bridges on the fracture properties. Gu et al. obtained slightly better fracture properties compared to this study [42].

Some previous literature studies showed a greater increase in fracture toughness compared to the fracture toughness of the individual constituents [11, 47]. The monolithic hard samples obtained a lower fracture toughness in these literature studies, resulting in a higher increase in fracture toughness compared to the individual constituents.

Slesarenko et al. showed that the fracture properties of previous studies are dependent on the

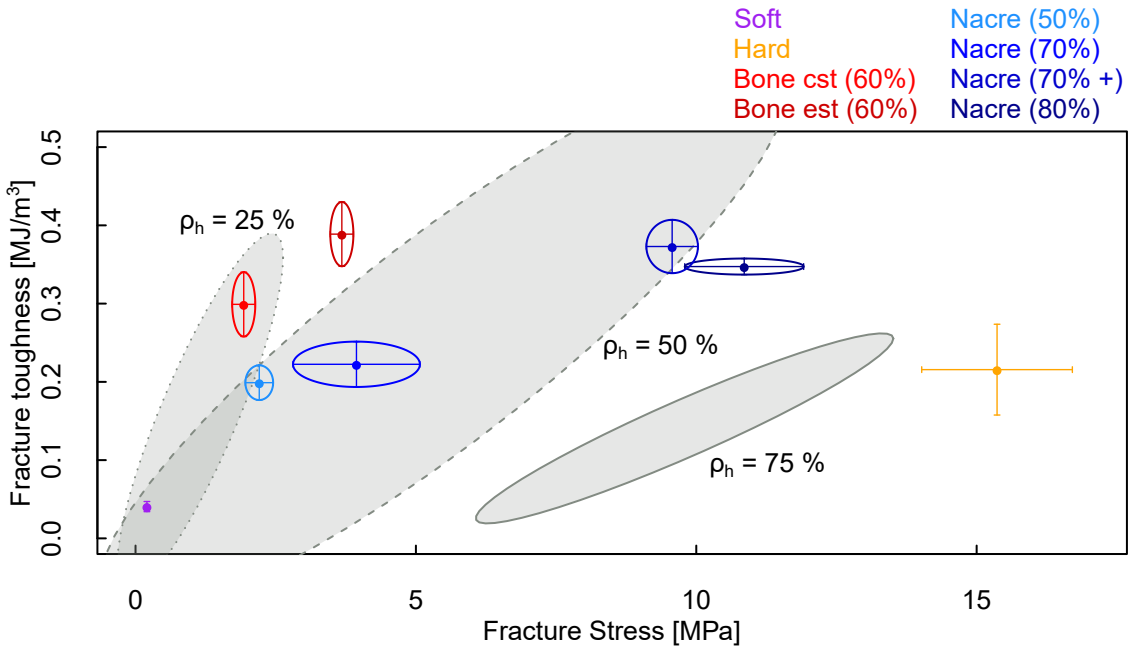


Figure 4.2: The graph compares the fracture stress and fracture toughness with previous literature studies. The grey 95 % confidence ellipses show the results obtained in this study for three different hard material ratios (75, 50 and 25). The two red ellipses show the bone-inspired results obtained by Libonati et al. [47]. Cst stands for circular soft osteons in a stiff matrix, whereas est stands for elliptical soft osteons in a stiff matrix. The four blue ellipses show the nacre-inspired results obtained by Gu et al. [42]. The + sign stands for mineral bridges. The hard material density is shown between parentheses in the legend.

inclination angle [44]. The hard-soft material arrangement was heterogeneously distributed in all directions in this study. As a result, the fracture properties would be less affected by the inclination angle compared to previous literature studies.

4.7.2. Nature

All the samples tested in this study showed toughening mechanisms, which where affected by the biomimetic design parameters. The samples showed crack deflection, crack bridging, crack blunting and crack branching (all extrinsic toughening mechanisms) and micro-crack formation (intrinsic toughening mechanism) [4, 47]. These toughening mechanisms are comparable to the toughening mechanisms of natural hard-soft materials. The soft material phases of the samples showed high deformations, whereas the hard material phases showed low deformations. The soft material deformations resulted in energy dissipation, which is comparable to energy dissipation by non-linear deformations in natural materials, such as nacre [4, 10, 14, 86]. Another toughening mechanism is crack deflection, which is active if the crack is trapped into the soft material phase [4, 6]. The samples printed at higher length scale exhibited more crack deflection. Furthermore, crack deflection was influenced by the hard-soft material arrangement and hard material ratio. Crack deflection is easier if higher amount of soft material is present. Figure 3.15b ($\rho_h = 25\%$) and Figure 3.16b ($\rho_h = 50\%$ and $\rho_h = 25\%$) show examples of crack deflection through the soft material phases. An example of crack deflection in natural materials is crack deflection in bone by osteons [47]. In addition to non-linear deformations and crack deflection, the soft material phases showed crack bridging during fracture. This toughening mechanism is comparable to collagen-fibril bridging in bone [47]. Another toughening mechanism of soft material phases is crack blunting, which reduces the sharpness of the crack tip. This toughening mechanism is comparable to crack blunting by soft material phases in tendon or nacre [5, 18, 87]. The toughening mechanism crack branching occurred during fracture of the $\rho_h = 75\%$ and monolithic hard material samples. Crack branching is an extrinsic toughening mechanism of bone [47]. Lastly, the fracture surfaces of the samples with a significant amount of soft material obtained micro-cracks. The formation of micro-cracks is also a toughening mechanism of bone [47].

4.8. Limitations and recommendations

This section describes different aspects that could have influenced the results of this study. First of all, the test set-up could have affected the fracture properties. The exact position of the PLA grippers could have been altered after a large repetition of tests. The grippers were slightly bended after all 138 tests were performed. Bending of the grippers has also been noticed in a previous literature study [47]. Some results were not consistent, indicating that the fracture properties were affected by the accuracy of the test set-up. Firstly, the fracture properties of some samples showed a high standard deviation, such as the fracture toughness of the semi-ordered $\rho_h = 50\%$ samples that were printed with a voxel-length of 40 and 240 μm. A high standard deviation, which was not required, shows that the test set-up was less accurate. However, only a few samples showed a relatively high standard deviation. Furthermore, the fracture toughness of the ordered $\rho_h = 50\%$ samples was higher for samples with a voxel-length of 480 μm compared to the samples with a voxel length of 240 μm. This was also due to the accuracy of the test set-up. Lastly, the stress-strain curves of the $\rho_h = 75\%$ samples showed a toe region at the beginning of the test, which was due to movement of the grippers at the beginning of the test. In addition, the stress-strain curves of the monolithic hard samples, which were tested with aluminium grippers, showed a toe region at the beginning of the test, which is also due to movement of the grippers. The aluminium grippers should be manufactured in exactly the right dimensions to prevent movement of the grippers. The aluminium grippers could not collapse or bend during testing. For this reason, aluminium grippers are recommended for upcoming tests to increase the accuracy of the test set-up.

The effect of biomimetic design parameters on fracture properties was only analysed with a tensile test. However, the effect of biomimetic design parameters could have been studied with computational modelling. Different hard-soft material arrangements could have been rapidly studied with a reliable computational model.

The hard-soft material arrangement was limited to three computer algorithms, including error diffusion, random and ordered dither. It was convenient to obtain a hard-soft arrangement in all directions with a computer algorithm.

Additionally, the manufacturing technique limited this study. The voxel size is limited by the resolution of the printer, which depends on the droplet size. It was not possible to print a voxel smaller than 40 x 80 x 32 μm. Furthermore, a limited type of materials is available for AM. There are not any biocompatible materials available. As a result, materials printed with an Objet500 Connex3 are not suitable for most medical applications, such as scaffold fabrication.

The sample thickness was 3 mm to maintain a similar geometry compared to previous studies. Consequently, the samples with a voxel length of 960 μm consisted of only three layers that differed in hard-soft material arrangement. Three layers is relatively small compared to the number of layers of the other samples. Crack arresting across the interface was more difficult for the samples with a voxel length of 960 μm (Figure 3.15).

The tests were not carried out subsequently. It is recommended to perform upcoming tests in sequence, to test all samples in exactly the same way. The influence of the test set-up on the fracture properties can be narrowed in this way. In addition, the time between printing and testing of the samples should be limited, considering that the material properties of the samples can degrade over time [88].

Every sample design was tested in triplex. It is recommended to test the samples in fivefold, because a statistical analysis about the effect of different biomimetic design parameters on fracture properties requires at least five samples. Furthermore, it is easier to identify outliers if more samples are tested.

Reference standards could not be used to obtain the fracture properties of the materials used for printing. The geometry and test set-up were similar to previous literature studies. An ASTM reference standard, in which aspects such as the displacement rate and sample geometry are set, will increase the similarity of future tests [79].

UV-curing of a hard-soft material interface could result in a third material [47]. The hard and soft materials mixed together at their interfaces, which could have influenced the fracture properties according to Voigt's rule of mixtures [37]. The precise effects of curing and mixing at a hard-soft material interface is unknown. These effects are higher for samples printed at native resolution. In addition, the liquidity of the material droplets, which affects the accuracy of the voxel dimensions, is also unknown. This effect is also larger at native resolution.

Various parameters, such as the process parameters, have an effect on the material properties of additively manufactured parts [80]. The samples were printed at exactly the same spot on the building tray to eliminate these effects. The manufacturing time can be decreased significantly if multiple samples are printed at the same time. However, the influence of the printing spot on the fracture properties is unknown.

4.9. Future research directions

Further research directions could improve the fracture properties of biomimetic hard-soft materials. The most important research directions include material hierarchy and anisotropy at different scales, hard-soft material interfaces and graded structures. These and other research directions are discussed below.

The hard-soft material arrangements were created with three different algorithms. These arrangements were based on the different structures of natural materials. It will be interesting to study additional hard-soft material arrangements. These arrangements can be designed based on the results of the algorithm-based arrangement analysed in this study. For instance, an inclined continuous structure of soft material, such as found in nacre, may increase the fracture toughness [4, 86].

In addition, the hard material ratio was analysed in this study. The hard material ratio of the hard-soft material samples was ranging between 25 and 75 %. The samples with a hard material ratio of 50 % showed the highest fracture toughness. However, a hard material ratio of 50 % is lower than the hard material ratio of most natural materials with a high fracture toughness. For example, the material ratio of hard organic bricks in nacre is 95 % [5, 74]. It will be interesting to study the effect of a hard material ratio of 85 % or 95 % on the fracture properties.

The length scale is the third biomimetic design parameter that has been analysed in this study. The results show that the samples printed at native resolution resulted in the highest fracture toughness values. Natural materials, such as bone, show a complex structure at different length scales, which results in toughening mechanisms at different length scales [1, 3, 4, 13, 19–25]. These length scales range from nano- to macro-scale [6]. It will be interesting to include samples that are composed of building blocks at different length scales in future research studies. The features of natural hard-soft materials are starting at nano-scale; making control over the nano-scale structure desirable for successful biomimetic design [30, 48, 49]. Additional research is required to improve the length scale that can be reached with AM while printing multiple materials together [89].

The stiffness ratio between the hard and soft material phases was kept equal to 921 in this study. Previous literature studies reported that the stiffness ratio should be at least five to let the soft material phases alleviate stress concentrations [11, 25, 32]. The stiffness ratio could range between five and 921 in future research studies. The stiffness ratio could be altered by making use of digital materials. It may be interesting to study the effect of different stiffness ratios on fracture properties.

Another interesting research field is the optimization of hard-soft materials by algorithm-driven designs [72, 90]. Gu et al. have optimized the hard-soft material arrangement with a greedy algorithm [72]. They increased the fracture toughness by 25 times compared to the toughness of the individual constituents [72]. Other design parameters, such as the length scale and hard-material ratios, can also be optimized with an algorithm.

This study did not include hard-soft material interfaces. The attachment of hard-soft materials is an interesting and important research topic [9, 17, 38, 46, 79]. Hard-soft material interfaces have different functions in nature, which can be categorized in: increasing the fracture resistance, attaching hard-soft materials and allowing material deformation and movement [17]. Natural hard-soft material interfaces have a high toughness compared to most artificial hard-soft material interfaces [91, 92]. The high toughness of natural interfaces is related to their structure. Natural hard-soft material interfaces often show a 'jigsaw' or wavy structure at the attachment site [45, 75]. It would be interesting to mimic these 'jigsaw' or wavy structures with AM. Furthermore, the enthesis, which anchors ligament or tendon to bone, and the osteochondral interface, which attaches cartilage to bone, show a graded structure. These natural graded structures could be mimicked with voxel-based AM, which is a well-suited technique for printing graded structures [93].

Besides the fracture properties, the effect of biomimetic design parameters on other material properties, such as the impact resistance, may be interesting to analyse as well [94]. Furthermore, the effect of loading conditions, including in-plane and transverse loadings, could be studied [95]. The

required material properties are dependent on the application of the material.

The computational modelling of biomimetic materials should become more precise [11, 36]. Achieving the same results with computational modelling, such as the finite element method (FEM), and practical analyses, such as a tensile test, is required [96]. Computational modelling could decrease the time it takes to analyse a biomimetic material. The strain concentrations in a FEM could be validated with strain concentrations that are obtained with DIC measurements [72]. Furthermore, the properties of AM structures can be tested to validate the properties obtained with computer models [3].

Voxel-based AM with a Polyjet printer enables the regulation of material deposition at micro-scale. This technique also enables the deposition of multiple materials, making the opportunities with voxel-based AM widespread [57]. Additional research is required to improve the print resolution of AM techniques, which enables printing at smaller length scale. Furthermore, the materials that are available for AM should be enlarged. For instance, materials available for an Objet500 Connex3 printer are restricted to photopolymers, which do not represent natural materials [3]. Research on applicable materials could improve the properties of biomimetic materials. A wider range of material properties could be achieved, if a wider range of materials is available for AM.

The improvement of biomimetic hard-soft materials and interfaces is relevant for a widespread of (medical) applications, including medical devices and biomaterials. Hard-soft tissue operations have a high failure rate, due to the inability to regenerate the complex structure of the native tissue interfaces, and due to the difficulty of attaching two materials with contradicting properties together at a low length scale [16, 28, 69, 97–99]. Future research on AM techniques and materials available for AM techniques is necessary to broaden the use of AM in clinical applications [12, 54]. For example, biomaterials should be biocompatible, and for some cases biodegradable [12]. MED610 materials, which are biocompatible, are available for the Connex3 printer [77]. However, there is only one type of bio-compatible material available for printing, whereas at least two types of biocompatible materials with contradicting properties are required to mimic natural composites.

The structure of natural materials, which outperform most artificial materials, were used as an example to design biomimetic materials with a high fracture toughness. Artificial materials have different boundary conditions and constraints compared to natural materials [33, 100]. For example, natural materials are limited by the the elements and ions found in their environment, whereas artificial materials do not have this constraint [100]. Research directions that could further improve the (fracture) properties of biomimetic materials are described in this section. The future will show if it is possible to manufacture materials with properties that are equal or superior to the properties of natural materials.

5

Conclusion

This study analysed the effect of three different biomimetic design parameters on the fracture properties of hard-soft material samples, that were fabricated using voxel-based AM. The isolated and modulated effects of the biomimetic design parameters on the stiffness, fracture stress, final strain and fracture toughness were studied to answer the main research question:

- **What are the isolated and modulated effects of the biomimetic design parameters, including length scale, hard material ratio and hard-soft material arrangement, on the fracture properties of biomimetic hard-soft materials?**

The fracture properties were affected by the biomimetic design parameters in a modulated way. In other words, the effect of a design parameter on a fracture property was influenced by the other design parameters. The fracture properties were mainly influenced by the length scale and hard material ratio. In general, a smaller amount of hard material resulted in a higher final strain, whereas a higher amount resulted in a higher stiffness and fracture stress. The monolithic hard samples obtained the highest stiffness and fracture stress. However, the fracture toughness of the hard-soft material samples could be increased by nearly two times compared to the toughness of the monolithic hard samples. The $\rho_h = 50\%$ samples with a voxel length of 40 μm obtained the highest fracture toughness, independently of the hard-soft material arrangement. The length scale had a greater effect on the fracture properties if a higher amount of soft material phases was present. Decreasing the length scale from 960 μm to native resolution could increase the fracture toughness by 1.7 to 5 times, depending on the hard material ratio and hard-soft material arrangement. Additionally, a decrease in length scale could increase the stiffness by 0.89 to 9.7 times and the fracture stress by 1.4 to 3.6 times. The effect of biomimetic design parameters on the fracture properties can be explained by the DIC measurements and the digital microscope images. The microscope images show that the fracture path tended to propagate through the soft material phases. Crack propagation through the soft material was more difficult at smaller length scale. DIC measurements show that the plasticity zone in front of the crack tip was larger for the samples printed at native resolution, resulting in a higher fracture toughness. The samples printed at a larger length scale showed more highly strained areas away from the crack tip instead of in front of the crack tip. The hard-soft material arrangement and hard material ratio influenced the crack path and strain distributions especially at a higher length scale, explaining the greater difference in fracture properties between the samples printed at a higher length scale.

The results are consistent with previous literature studies that used the same printer and a similar test set-up. This study supports the potential of biomimetic design parameters in improving hard-soft materials, which could be used in a widespread of applications. Furthermore, this study shows that the fracture properties of hard-soft materials could be regulated by adjusting the length scale, hard material ratio and hard-soft material arrangement. Additional research on biomimetic designs could further enhance the fracture properties of hard-soft materials. Lastly, further research on AM could improve the length scale that can be achieved with AM techniques and improve the diversity in materials that are available for AM.

Bibliography

[1] M. E. Launey and R. O. Ritchie, “On the fracture toughness of advanced materials,” Advanced Materials, vol. 21, no. 20, pp. 2103–2110, 2009.

[2] R. O. Ritchie, “The conflicts between strength and toughness,” Nature materials, vol. 10, no. 11, pp. 817–822, 2011.

[3] G. X. Gu, I. Su, S. Sharma, J. L. Voros, Z. Qin, and M. J. Buehler, “Three-dimensional-printing of bio-inspired composites,” Journal of biomechanical engineering, vol. 138, no. 2, p. 021006, 2016.

[4] F. Libonati and M. J. Buehler, “Advanced structural materials by bioinspiration,” Advanced Engineering Materials, 2017.

[5] K. Okumura and P.-G. De Gennes, “Why is nacre strong? elastic theory and fracture mechanics for biocomposites with stratified structures,” The European Physical Journal E: Soft Matter and Biological Physics, vol. 4, no. 1, pp. 121–127, 2001.

[6] F. Barthelat, “Architectured materials in engineering and biology: fabrication, structure, mechanics and performance,” International Materials Reviews, vol. 60, no. 8, pp. 413–430, 2015.

[7] A. R. Studart, “Biological and bioinspired composites with spatially tunable heterogeneous architectures,” Advanced Functional Materials, vol. 23, no. 36, pp. 4423–4436, 2013.

[8] A. R. Studart, “Additive manufacturing of biologically-inspired materials,” Chemical Society Reviews, vol. 45, no. 2, pp. 359–376, 2016.

[9] Z. Liu, M. A. Meyers, Z. Zhang, and R. O. Ritchie, “Functional gradients and heterogeneities in biological materials: Design principles, functions, and bioinspired applications,” Progress in Materials Science, vol. 88, pp. 467–498, 2017.

[10] U. G. Wegst, H. Bai, E. Saiz, A. P. Tomsia, and R. O. Ritchie, “Bioinspired structural materials,” Nature materials, vol. 14, no. 1, p. 23, 2015.

[11] L. S. Dimas, G. H. Bratzel, I. Eylon, and M. J. Buehler, “Tough composites inspired by mineralized natural materials: computation, 3d printing, and testing,” Advanced Functional Materials, vol. 23, no. 36, pp. 4629–4638, 2013.

[12] A. A. Zadpoor, “Design for additive bio-manufacturing: From patient-specific medical devices to rationally designed meta-biomaterials,” International journal of molecular sciences, vol. 18, no. 8, p. 1607, 2017.

[13] M. E. Launey, M. J. Buehler, and R. O. Ritchie, “On the mechanistic origins of toughness in bone,” Annual review of materials research, vol. 40, pp. 25–53, 2010.

[14] M. A. Meyers, J. McKittrick, and P.-Y. Chen, “Structural biological materials: critical mechanics-materials connections,” science, vol. 339, no. 6121, pp. 773–779, 2013.

[15] P. J. Yang and J. S. Temenoff, “Engineering orthopedic tissue interfaces,” Tissue Engineering Part B: Reviews, vol. 15, no. 2, pp. 127–141, 2009.

[16] O. E. Armitage and M. L. Oyen, “Hard-soft tissue interface engineering,” in Engineering Mineralized and Load Bearing Tissues, pp. 187–204, Springer, 2015.

[17] J. W. Dunlop, R. Weinkamer, and P. Fratzl, “Artful interfaces within biological materials,” Materials Today, vol. 14, no. 3, pp. 70–78, 2011.

[18] F. Barthelat, Z. Yin, and M. J. Buehler, “Structure and mechanics of interfaces in biological materials,” Nature Reviews Materials, vol. 1, no. 4, p. 16007, 2016.

[19] O. Tokareva, M. Jacobsen, M. Buehler, J. Wong, and D. L. Kaplan, “Structure–function–property–design interplay in biopolymers: Spider silk,” Acta biomaterialia, vol. 10, no. 4, pp. 1612–1626, 2014.

[20] R. Wang, Z. Suo, A. Evans, N. Yao, and I. Aksay, “Deformation mechanisms in nacre,” Journal of Materials Research, vol. 16, no. 9, pp. 2485–2493, 2001.

[21] P.-Y. Chen, A. Lin, Y.-S. Lin, Y. Seki, A. Stokes, J. Peyras, E. Olevsky, M. Meyers, and J. McKittrick, “Structure and mechanical properties of selected biological materials,” Journal of the Mechanical Behavior of Biomedical Materials, vol. 1, no. 3, pp. 208–226, 2008.

[22] M. A. Meyers, P.-Y. Chen, A. Y.-M. Lin, and Y. Seki, “Biological materials: structure and mechanical properties,” Progress in Materials Science, vol. 53, no. 1, pp. 1–206, 2008.

[23] S. Bechtle, S. F. Ang, and G. A. Schneider, “On the mechanical properties of hierarchically structured biological materials,” Biomaterials, vol. 31, no. 25, pp. 6378–6385, 2010.

[24] Z. Zhang, Y.-W. Zhang, and H. Gao, “On optimal hierarchy of load-bearing biological materials,” Proceedings of the Royal Society of London B: Biological Sciences, vol. 278, no. 1705, pp. 519–525, 2011.

[25] F. Barthelat, “Designing nacre-like materials for simultaneous stiffness, strength and toughness: Optimum materials, composition, microstructure and size,” Journal of the Mechanics and Physics of Solids, vol. 73, pp. 22–37, 2014.

[26] O. Kolednik, J. Predan, F. D. Fischer, and P. Fratzl, “Bioinspired design criteria for damage-resistant materials with periodically varying microstructure,” Advanced Functional Materials, vol. 21, no. 19, pp. 3634–3641, 2011.

[27] F. Barthelat, C.-M. Li, C. Comi, and H. D. Espinosa, “Mechanical properties of nacre constituents and their impact on mechanical performance,” Journal of Materials Research, vol. 21, no. 8, pp. 1977–1986, 2006.

[28] H. H. Lu and S. Thomopoulos, “Functional attachment of soft tissues to bone: development, healing, and tissue engineering,” Annual review of biomedical engineering, vol. 15, pp. 201–226, 2013.

[29] A. Prabhath, V. N. Vernekar, E. Sanchez, and C. T. Laurencin, “Growth factor delivery strategies for rotator cuff repair and regeneration,” International journal of pharmaceutics, 2018.

[30] H. Gao, B. Ji, I. L. Jäger, E. Arzt, and P. Fratzl, “Materials become insensitive to flaws at nanoscale: lessons from nature,” Proceedings of the national Academy of Sciences, vol. 100, no. 10, pp. 5597–5600, 2003.

[31] B. Ji and H. Gao, “Mechanical properties of nanostructure of biological materials,” Journal of the Mechanics and Physics of Solids, vol. 52, no. 9, pp. 1963–1990, 2004.

[32] P. Fratzl, H. S. Gupta, F. D. Fischer, and O. Kolednik, “Hindered crack propagation in materials with periodically varying young’s modulus—lessons from biological materials,” Advanced Materials, vol. 19, no. 18, pp. 2657–2661, 2007.

[33] J. Aizenberg and P. Fratzl, “Biological and biomimetic materials,” Advanced Materials, vol. 21, no. 4, pp. 387–388, 2009.

[34] D. Sen and M. J. Buehler, “Structural hierarchies define toughness and defect-tolerance despite simple and mechanically inferior brittle building blocks,” Scientific reports, vol. 1, p. 35, 2011.

[35] L. S. Dimas and M. J. Buehler, “Influence of geometry on mechanical properties of bio-inspired silica-based hierarchical materials,” Bioinspiration & biomimetics, vol. 7, no. 3, p. 036024, 2012.

[36] L. S. Dimas and M. J. Buehler, “Tough and stiff composites with simple building blocks,” Journal of Materials Research, vol. 28, no. 10, pp. 1295–1303, 2013.

[37] L. S. Dimas and M. J. Buehler, “Modeling and additive manufacturing of bio-inspired composites with tunable fracture mechanical properties,” Soft Matter, vol. 10, no. 25, pp. 4436–4442, 2014.

[38] E. Lin, Y. Li, C. Ortiz, and M. C. Boyce, “3d printed, bio-inspired prototypes and analytical models for structured suture interfaces with geometrically-tuned deformation and failure behavior,” Journal of the Mechanics and Physics of Solids, vol. 73, pp. 166–182, 2014.

[39] R. Mirzaeifar, L. S. Dimas, Z. Qin, and M. J. Buehler, “Defect-tolerant bioinspired hierarchical composites: simulation and experiment,” ACS Biomaterials Science & Engineering, vol. 1, no. 5, pp. 295–304, 2015.

[40] L. Djumas, A. Molotnikov, G. P. Simon, and Y. Estrin, “Enhanced mechanical performance of bio-inspired hybrid structures utilising topological interlocking geometry,” Scientific reports, vol. 6, p. 26706, 2016.

[41] G. X. Gu, L. Dimas, Z. Qin, and M. J. Buehler, “Optimization of composite fracture properties: Method, validation, and applications,” Journal of Applied Mechanics, vol. 83, no. 7, p. 071006, 2016.

[42] G. X. Gu, F. Libonati, S. D. Wettermark, and M. J. Buehler, “Printing nature: Unraveling the role of nacre’s mineral bridges,” Journal of the mechanical behavior of biomedical materials, vol. 76, pp. 135–144, 2017.

[43] L. Djumas, G. P. Simon, Y. Estrin, and A. Molotnikov, “Deformation mechanics of non-planar topologically interlocked assemblies with structural hierarchy and varying geometry,” Scientific reports, vol. 7, no. 1, p. 11844, 2017.

[44] V. Slesarenko, N. Kazarinov, and S. Rudykh, “Distinct failure modes in bio-inspired 3d-printed staggered composites under non-aligned loadings,” Smart Materials and Structures, vol. 26, no. 3, p. 035053, 2017.

[45] I. Malik, M. Mirkhalaf, and F. Barthelat, “Bio-inspired “jigsaw”-like interlocking sutures: Modeling, optimization, 3d printing and testing,” Journal of the Mechanics and Physics of Solids, vol. 102, pp. 224–238, 2017.

[46] Y. Zhang, H. Yao, C. Ortiz, J. Xu, and M. Dao, “Bio-inspired interfacial strengthening strategy through geometrically interlocking designs,” journal of the mechanical behavior of biomedical materials, vol. 15, pp. 70–77, 2012.

[47] F. Libonati, G. X. Gu, Z. Qin, L. Vergani, and M. J. Buehler, “Bone-inspired materials by design: Toughness amplification observed using 3d printing and testing,” Advanced Engineering Materials, vol. 18, no. 8, pp. 1354–1363, 2016.

[48] F. Hanßke, O. Bas, C. Vaquette, G. Hochleitner, J. Groll, E. Kemnitz, D. W. Hutmacher, and H. G. Börner, “Via precise interface engineering towards bioinspired composites with improved 3d printing processability and mechanical properties,” Journal of Materials Chemistry B, vol. 5, no. 25, pp. 5037–5047, 2017.

[49] R. Yadav, M. Naebe, X. Wang, and B. Kandasubramanian, “Review on 3d prototyping of damage tolerant interdigitating brick arrays of nacre,” Industrial & Engineering Chemistry Research, vol. 56, no. 38, pp. 10516–10525, 2017.

[50] Y. Zeng, Y. Yan, H. Yan, C. Liu, P. Li, P. Dong, Y. Zhao, and J. Chen, “3d printing of hydroxyapatite scaffolds with good mechanical and biocompatible properties by digital light processing,” Journal of Materials Science, pp. 1–11.

[51] W. Zhang, Q. Lian, D. Li, K. Wang, D. Hao, W. Bian, and Z. Jin, “The effect of interface microstructure on interfacial shear strength for osteochondral scaffolds based on biomimetic design and 3d printing,” Materials Science and Engineering: C, vol. 46, pp. 10–15, 2015.

[52] R. R. Jose, M. J. Rodriguez, T. A. Dixon, F. Omenetto, and D. L. Kaplan, “Evolution of bioinks and additive manufacturing technologies for 3d bioprinting,” ACS Biomaterials Science & Engineering, vol. 2, no. 10, pp. 1662–1678, 2016.

[53] W. Zhu, X. Ma, M. Gou, D. Mei, K. Zhang, and S. Chen, “3d printing of functional biomaterials for tissue engineering,” Current opinion in biotechnology, vol. 40, pp. 103–112, 2016.

[54] A. A. Zadpoor and J. Malda, “Additive manufacturing of biomaterials, tissues, and organs,” 2017.

[55] D. Kokkinis, F. Bouville, and A. R. Studart, “3d printing of materials with tunable failure via bioinspired mechanical gradients,” Advanced Materials, 2018.

[56] D. Kokkinis, M. Schaffner, and A. R. Studart, “Multimaterial magnetically assisted 3d printing of composite materials,” Nature communications, vol. 6, p. 8643, 2015.

[57] J. J. Martin, B. E. Fiore, and R. M. Erb, “Designing bioinspired composite reinforcement architectures via 3d magnetic printing,” Nature communications, vol. 6, p. 8641, 2015.

[58] S. Deville, E. Saiz, R. K. Nalla, and A. P. Tomsia, “Freezing as a path to build complex composites,” Science, vol. 311, no. 5760, pp. 515–518, 2006.

[59] E. Munch, M. E. Launey, D. H. Alsem, E. Saiz, A. P. Tomsia, and R. O. Ritchie, “Tough, bioinspired hybrid materials,” Science, vol. 322, no. 5907, pp. 1516–1520, 2008.

[60] H. Bai, F. Walsh, B. Gludovatz, B. Delattre, C. Huang, Y. Chen, A. P. Tomsia, and R. O. Ritchie, “Bioinspired hydroxyapatite/poly (methyl methacrylate) composite with a nacre-mimetic architecture by a bidirectional freezing method,” Advanced Materials, vol. 28, no. 1, pp. 50–56, 2016.

[61] R. P. Wilkerson, B. Gludovatz, J. Watts, A. P. Tomsia, G. E. Hilmas, and R. O. Ritchie, “A novel approach to developing biomimetic (“nacre-like”) metal-compliant-phase (nickel–alumina) ceramics through coextrusion,” Advanced Materials, vol. 28, no. 45, pp. 10061–10067, 2016.

[62] P. Podsiadlo, A. K. Kaushik, E. M. Arruda, A. M. Waas, B. S. Shim, J. Xu, H. Nandivada, B. G. Pumplin, J. Lahann, A. Ramamoorthy, et al., “Ultrastrong and stiff layered polymer nanocomposites,” Science, vol. 318, no. 5847, pp. 80–83, 2007.

[63] A. Finnemore, P. Cunha, T. Shean, S. Vignolini, S. Guldin, M. Oyen, and U. Steiner, “Biomimetic layer-by-layer assembly of artificial nacre,” Nature communications, vol. 3, p. 966, 2012.

[64] F. Libonati, C. Colombo, and L. Vergani, “Design and characterization of a biomimetic composite inspired to human bone,” Fatigue & Fracture of Engineering Materials & Structures, vol. 37, no. 7, pp. 772–781, 2014.

[65] T. Guillén, Q.-H. Zhang, G. Tozzi, A. Ohrndorf, H.-J. Christ, and J. Tong, “Compressive behaviour of bovine cancellous bone and bone analogous materials, microct characterisation and fe analysis,” Journal of the mechanical behavior of biomedical materials, vol. 4, no. 7, pp. 1452–1461, 2011.

[66] M. J. Mirzaali, V. Mussi, P. Vena, F. Libonati, L. Vergani, and M. Strano, “Mimicking the loading adaptation of bone microstructure with aluminum foams,” Materials & Design, vol. 126, pp. 207–218, 2017.

[67] M. Mirkhalaf, A. K. Dastjerdi, and F. Barthelat, “Overcoming the brittleness of glass through bio-inspiration and micro-architecture,” Nature communications, vol. 5, p. 3166, 2014.

[68] F. Libonati and L. Vergani, “Cortical bone as a biomimetic model for the design of new composites,” Procedia Structural Integrity, vol. 2, pp. 1319–1326, 2016.

[69] N. Lee, J. Robinson, and H. Lu, “Biomimetic strategies for engineering composite tissues,” Current opinion in biotechnology, vol. 40, pp. 64–74, 2016.

[70] O. Zoran, "Multi-material voxel based 3d printing." http://www.ernw.ac.uk/getfile.php?type=site_documents&id=IDTechEx_Europe2016PresentationStratasys%20-%20multi%20material%20voxel%20based%203D%20printing.pdf, 2016 (accessed January 8, 2018).

[71] T. Swetly, J. Stampfl, G. Kempf, R.-M. Hucke, M. Willing, and M. Warkentin, "Bioinspired engineering polymers by voxel-based 3d-printing," BioNanoMaterials, vol. 17, no. 3-4, pp. 145–157, 2016.

[72] G. X. Gu, S. Wettermark, and M. J. Buehler, "Algorithm-driven design of fracture resistant composite materials realized through additive manufacturing," Additive Manufacturing, vol. 17, pp. 47–54, 2017.

[73] X. Feng, "Chemical and biochemical basis of cell-bone matrix interaction in health and disease," Current chemical biology, vol. 3, no. 2, pp. 189–196, 2009.

[74] J. Sun and B. Bhushan, "Hierarchical structure and mechanical properties of nacre: a review," Rsc Advances, vol. 2, no. 20, pp. 7617–7632, 2012.

[75] H. D. Espinosa, J. E. Rim, F. Barthelat, and M. J. Buehler, "Merger of structure and material in nacre and bone–perspectives on de novo biomimetic materials," Progress in Materials Science, vol. 54, no. 8, pp. 1059–1100, 2009.

[76] G. M. Genin, A. Kent, V. Birman, B. Wopenka, J. D. Pasteris, P. J. Marquez, and S. Thomopoulos, "Functional grading of mineral and collagen in the attachment of tendon to bone," Biophysical journal, vol. 97, no. 4, pp. 976–985, 2009.

[77] Stratasys, "Objet500 and objet350 connex3." http://www.stratasys.com/3d-printers/production-series/connex3-systems, 2014 (accessed January 8, 2018).

[78] K. corporation, "Digital microscope - vhx-5000 series." https://www.keyence.com/products/microscope/digital-microscope/vhx-5000/index.jsp, 2018 (accessed April 17, 2018).

[79] I. Vu, L. Bass, N. Meisel, B. Orler, C. B. Williams, and D. A. Dillard, "Characterization of mutlimaterial interfaces in polyjet additive manufacturing," in Solid Freeform Fabrication Symposium, pp. 959–982, 2014.

[80] J. Mueller, K. Shea, and C. Daraio, "Mechanical properties of parts fabricated with inkjet 3d printing through efficient experimental design," Materials & Design, vol. 86, pp. 902–912, 2015.

[81] E. Doubrovski, E. Tsai, D. Dikovsky, J. Geraedts, H. Herr, and N. Oxman, "Voxel-based fabrication through material property mapping: A design method for bitmap printing," Computer-Aided Design, vol. 60, pp. 3–13, 2015.

[82] A. Standard et al., "Standard test methods for plane-strain fracture toughness and strain energy release rate of plastic materials," Annul Book of ASTM Standards, vol. 14, 1996.

[83] L. FLOYD, "An adaptive algorithm for spatial greyscale," in Proc. of the SID, vol. 17, pp. 75–77, 1976.

[84] W. Cho, E. M. Sachs, N. M. Patrikalakis, and D. E. Troxel, "A dithering algorithm for local composition control with three-dimensional printing," Computer-aided design, vol. 35, no. 9, pp. 851–867, 2003.

[85] J. Morris Jr, "A survey of a survey of materials science materials science iv. mechanical properties iv. mechanical properties," University of California, Berkeley, 2008.

[86] P. Fratzl, I. Burgert, and H. S. Gupta, "On the role of interface polymers for the mechanics of natural polymeric composites," Physical Chemistry Chemical Physics, vol. 6, no. 24, pp. 5575–5579, 2004.

[87] R. F. Ker, "Mechanics of tendon, from an engineering perspective," International Journal of Fatigue, vol. 29, no. 6, pp. 1001–1009, 2007.

[88] C. A. Costa, P. R. Linzmaier, and F. M. Pasquali, “Rapid prototyping material degradation: a study of mechanical properties,” IFAC Proceedings Volumes, vol. 46, no. 24, pp. 350–355, 2013.

[89] S. C. Ligon, R. Liska, J. Stampfl, M. Gurr, and R. Mülhaupt, “Polymers for 3d printing and customized additive manufacturing,” 2017.

[90] G. X. Gu, C.-T. Chen, and M. J. Buehler, “De novo composite design based on machine learning algorithm,” Extreme Mechanics Letters, vol. 18, pp. 19–28, 2018.

[91] Y. Liu, V. Birman, C. Chen, S. Thomopoulos, and G. M. Genin, “Mechanisms of bimaterial attachment at the interface of tendon to bone,” Journal of engineering materials and technology, vol. 133, no. 1, p. 011006, 2011.

[92] Y. Liu, S. Thomopoulos, V. Birman, J.-S. Li, and G. M. Genin, “Bi-material attachment through a compliant interfacial system at the tendon-to-bone insertion site,” Mechanics of Materials, vol. 44, pp. 83–92, 2012.

[93] Z. Liu, Y. Zhu, D. Jiao, Z. Weng, Z. Zhang, and R. O. Ritchie, “Enhanced protective role in materials with gradient structural orientations: Lessons from nature,” Acta biomaterialia, vol. 44, pp. 31–40, 2016.

[94] G. X. Gu, M. Takaffoli, A. J. Hsieh, and M. J. Buehler, “Biomimetic additive manufactured polymer composites for improved impact resistance,” Extreme Mechanics Letters, vol. 9, pp. 317–323, 2016.

[95] P. Tran, T. D. Ngo, A. Ghazlan, and D. Hui, “Bimaterial 3d printing and numerical analysis of bio-inspired composite structures under in-plane and transverse loadings,” Composites Part B: Engineering, vol. 108, pp. 210–223, 2017.

[96] A. E. Vellwock, L. Vergani, and F. Libonati, “A multiscale xfem approach to investigate the fracture behavior of bio-inspired composite materials,” Composites Part B: Engineering, 2018.

[97] A. Seidi, M. Ramalingam, I. Elloumi-Hannachi, S. Ostrovidov, and A. Khademhosseini, “Gradient biomaterials for soft-to-hard interface tissue engineering,” Acta biomaterialia, vol. 7, no. 4, pp. 1441–1451, 2011.

[98] F. Saadat, A. C. Deymier, V. Birman, S. Thomopoulos, and G. M. Genin, “The concentration of stress at the rotator cuff tendon-to-bone attachment site is conserved across species,” Journal of the mechanical behavior of biomedical materials, vol. 62, pp. 24–32, 2016.

[99] L. M. Galatz, C. M. Ball, S. A. Teefey, W. D. Middleton, and K. Yamaguchi, “The outcome and repair integrity of completely arthroscopically repaired large and massive rotator cuff tears,” JBJS, vol. 86, no. 2, pp. 219–224, 2004.

[100] G. Mayer, “Rigid biological systems as models for synthetic composites,” Science, vol. 310, no. 5751, pp. 1144–1147, 2005.

A

Fracture properties

Table A.1: The fracture properties of semi-ordered samples with a hard material ratio of 75, 50 and 25 %. The mean value and standard deviation are given.

	Semi-ordered											
ρ_h [%]	75				50				25			
Length scale [μm]	40	240	480	960	40	240	480	960	40	240	480	960
E [MPa]	401 ±51	393 ±53	357 ±11	449 ±7.4	267 ±41	249 ±12	145 ±7.8	120 ±8.5	43.4 ±1.7	16.6 ±0.5	10.2 ±1.5	16.6 ±0.5
σ_f [MPa]	11.2 ±0.6	10.5 ±0.1	9.69 ±0.3	8.95 ±0.2	7.95 ±2.0	7.54 ±0.4	4.00 ±0.2	2.74 ±.02	0.59 ±.02	1.39 ±.03	1.11 ±.04	0.59 ±.02
ϵ_f [%]	3.60 ±0.2	3.36 ±0.4	3.34 ±0.3	2.56 ±.05	8.68 ±4.2	7.01 ±1.5	9.07 ±0.2	6.60 ±0.6	18.5 ±0.6	21.4 ±1.0	25.4 ±0.5	27.5 ±0.8
U [MJ/m^3]	0.20 ±.01	0.17 ±.03	0.16 ±.02	0.10 ±.00	0.40 ±.10	0.34 ±.06	0.25 ±.01	0.12 ±.01	0.27 ±.01	0.19 ±.01	0.17 ±.01	0.12 ±.01

Table A.2: The fracture properties of semi-ordered samples with a hard material ratio of 62 and 38 %. The mean value and standard deviation are given.

	Semi-ordered							
ρ_h [%]	62				38			
Length scale [µm]	40	240	480	960	40	240	480	960
E [MPa]	411 ±38	356 ±21	309 ±30	288 ±24	135 ±12	98.2 ±10	65.6 ±7.3	98.2 ±10
σ_f [MPa]	11.5 ±0.9	9.66 ±0.3	7.22 ±0.7	7.21 ±0.5	1.26 ±0.1	3.73 ±0.2	2.42 ±0.1	1.26 ±0.1
ϵ_f [%]	3.90 ±0.2	3.62 ±0.4	3.18 ±0.1	3.43 ±0.2	15.0 ±0.2	14.9 ±0.3	15.7 ±2.5	17.5 ±1.3
U [MJ/m^3]	0.22 ±.01	0.18 ±.03	0.11 ±.02	0.13 ± .01	0.39 ±.02	0.38 ± .02	0.21 ±.01	0.10 ±.02

Table A.3: The fracture properties of random arranged samples. The mean value and standard deviation are given.

Random												
ρ_h [%]	75				50				25			
Length scale [μm]	40	240	480	960	40	240	480	960	40	240	480	960
E [MPa]	416 ± 23	429 ±15	412 ±11	425 ±27	253 ±8.3	211 ±1.3	194 ±14	126 ±8.0	34.8 ±0.9	18.8 ±1.4	13.1 ±0.5	7.38 ±0.7
σ_f [MPa]	11.6 ±0.2	9.05 ±0.5	10.1 ±0.8	7.34 ±0.3	7.69 ±0.6	5.59 ±0.2	4.18 ±0.2	2.28 ±0.4	1.82 ±0.1	1.31 ±.02	0.92 ±.03	0.50 ±.01
ϵ_f [%]	3.61 ±0.3	2.55 ±0.3	2.96 ±0.2	2.40 ±0.2	8.06 ±1.1	4.68 ±0.2	4.75 ±0.2	10.9 0.8	20.9 ±0.9	19.1 ±0.2	29.7 ±0.9	24.0 ±3.7
U [MJ/m^3]	0.21 ±.02	0.11 ±.01	0.14 ±.02	0.07 ±.01	0.40 ±.04	0.16 ±.01	0.13 ±.01	0.08 ±.03	0.26 ±.01	0.16 ±.01	0.15 ±.00	0.07 ±.01

Table A.4: The fracture properties of ordered arranged samples. The mean value and standard deviation are given.

Ordered												
ρ_h [%]	75				50				25			
Length scale [μm]	40	240	480	960	40	240	480	960	40	240	480	960
E [MPa]	430 ±6.0	414 ±14	446 ±5.1	406 ±15	270 ±8.6	266 ±12	218 ±4.0	153 ±6.6	52.6 ±2.8	32.7 ±4.1	12.3 ±0.5	5.40 ±0.3
σ_f [MPa]	11.2 ±0.2	10.2 ±0.4	10.1 ±0.5	7.74 ±0.7	7.25 ±0.2	7.82 ±0.1	5.57 ±0.2	2.96 ±0.3	1.43 ±0.1	147 ±.04	0.70 ±.03	0.48 ±.02
ϵ_f [%]	3.20 ±.06	3.03 ±0.1	2.72 ±0.2	2.33 ±0.3	8.90 ±0.2	5.74 ±0.6	8.86 ±0.2	6.53 ±0.6	27.6 ±1.1	13.7 ±0.9	15.1 ±0.6	21.4 ±1.9
U [MJ/m^3]	0.17 ±.00	0.15 ±.01	0.13 ±.01	0.09 ±.02	0.41 ±.01	0.29 ±.03	0.32 ±.01	0.13 ±.02	0.30 ±.02	0.13 ±.00	0.07 ±.01	0.06 ±.00

B

Digital image correlation images

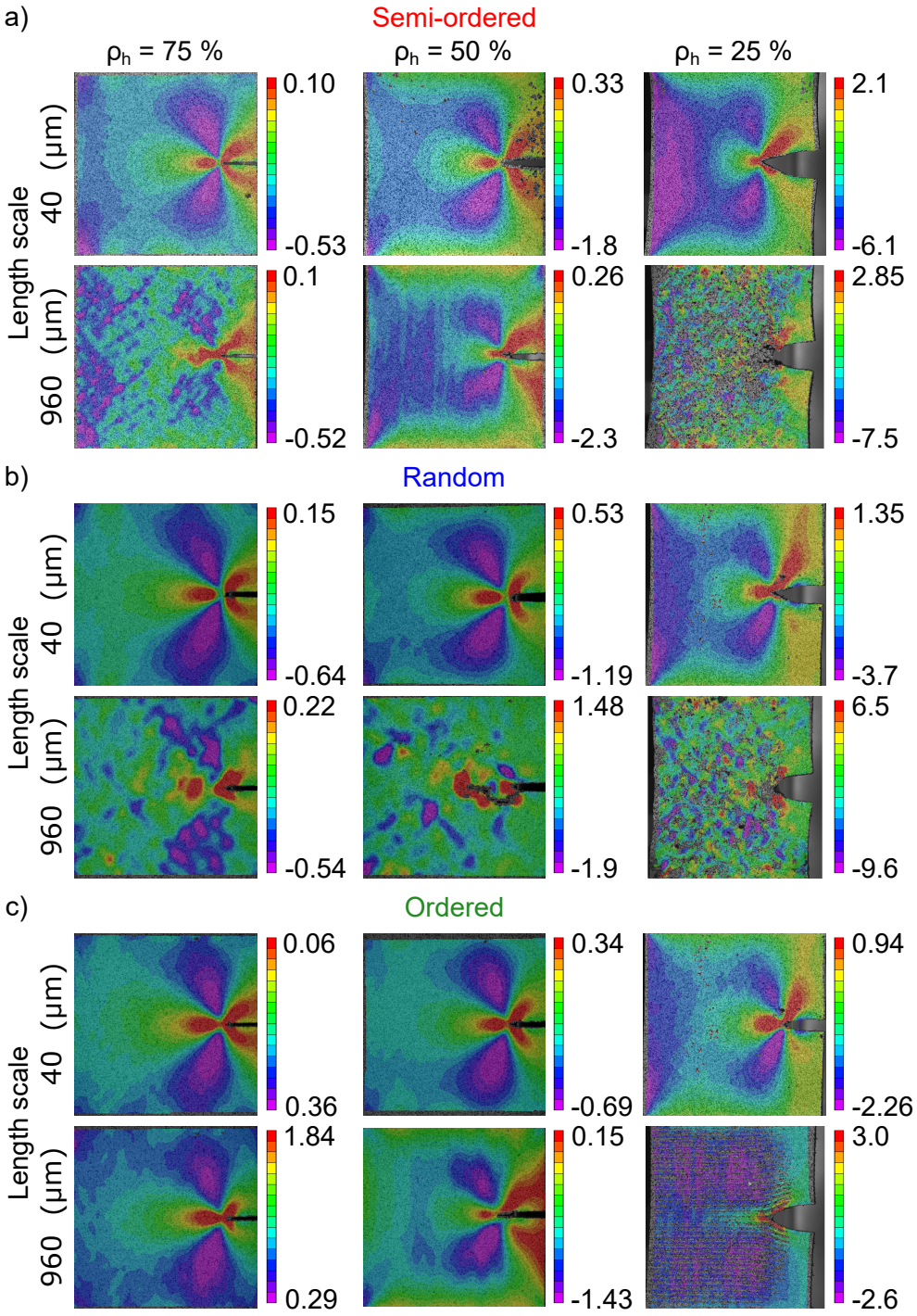


Figure B.1: Strain distribution in the X-direction at the moment of maximum applied force for a semi-ordered (a), random (b) and ordered (c) arrangement. The strain distributions are shown for different hard material ratios and two different length scales (40 and 960 μm). The minimum and maximum strain values are given in percentages.